Extremely large-amplitude dynamics of cantilevers under coupled base excitation

Hamed Farokhi [a], Mergen H. Ghayesh [b,*]

[a] *Department of Mechanical and Construction Engineering, Northumbria University, Newcastle upon Tyne NE1 8ST, UK*
[b] *School of Mechanical Engineering, University of Adelaide, South Australia 5005, Australia*
**Corresponding author: mergen.ghayesh@adelaide.edu.au*
Email: (H Farokhi): hamed.farokhi@northumbria.ac.uk

Abstract

Extremely large-amplitude nonlinear dynamics of a cantilever with a mass at the tip under coupled base excitations is examined for the first time. An exact model of the centreline rotation of the cantilever is developed capable of accurately predicting the cantilever dynamic response even at extremely large amplitudes; a nonlinear static finite element analysis is conducted to verify the accuracy of the proposed model at very large deflection amplitudes. The proposed model is based on the theory of Euler-Bernoulli and the internal damping model of Kelvin-Voigt; the centreline of the cantilever is assumed to remain inextensible. The proposed model for the cantilever centreline rotation is discretised via the Galerkin modal decomposition method while keeping all terms exact. Extensive numerical simulations are conducted to examine the primary and parametric resonance of the cantilever due to transverse and axial base excitations, respectively. It is shown that under the same axial and transverse amplitudes of excitation, the parametric resonance is much stronger than the primary resonance.

Keywords: Extremely large-amplitude dynamics; Cantilever; Coupled base excitation; Primary and parametric resonances; Kelvin-Voigt

1. Introduction

Beams and plates are present in various engineering systems and applications ranging from macro to micro scales (AkhavanAlavi et al., 2019; Ashoori Movassagh and Mahmoodi, 2013; Basutkar et al., 2019; Ghayesh et al., 2017; Gusella et al., 2019; Li et al., 2019; Mirsalehi et al., 2017; Mitchell and Gau, 2019; Nampally et al., 2019; Reddy et al., 2016; Rokni et al., 2015; Ruzziconi et al., 2013; Sadeghmanesh et al., 2019; Talimian and Béda, 2018; Wang et al., 2011; Xu and Deng, 2016; Zhang et al., 2013). Cantilevered beams are commonly subject to base excitations in axial, transverse, or both directions. Cantilevers can be found, for instance, in scanning probe microscopy, micro/nano resonators, mass sensors, vibration-based energy harvesters, and micro/nano-electromechanical systems (Farokhi et al., 2013; Friswell et al., 2012; Ghayesh et al., 2013b; Ghayesh and Farokhi, 2015a, b; Ghayesh et al., 2016; Ghayesh et al., 2013c, 2014; Gholipour et al., 2015; Kumar et al., 2011; Liu et al., 2012; Mahmoodi and Jalili, 2007). One of the unique features of cantilevers is that they can undergo deformations/vibrations (Ghayesh, 2012; Ghayesh and Moradian, 2011; Ghayesh et al., 2010; Karimi, 2006; Palacios-Quiñonero et al., 2012; Si et al., 2014) of extremely large amplitude due to having one end free. The other feature of cantilevers, resulting again from having one free end, is that the axial strain developed in the midplane of the cantilever is almost zero, allowing for application of a realistic assumption known as the centreline inextensibility. This is significantly important as it allows for describing the transverse and axial motions of the cantilever in terms of the midplane rotation; this will be explained in more detail in Section 2. One of the major difficulties associated with modelling and analysis of cantilevers undergoing large-amplitude motions is the presence of various sources of nonlinearity, namely geometric nonlinearities

due to large rotations, inertial-type nonlinearities, and damping nonlinearities. But the most difficult challenge in analysing cantilevers is capturing very large-amplitude responses when the tip angle grows larger than 90°. Such challenges in modelling and analysis of cantilevers have motivated a large amount of research on this topic. In what follows, a summarised review of the literature is presented.

Cantilevers statics and dynamics have been the topic of investigation over the past few decades. Early studies on this topic were conducted by Crespo da Silva and Glynn (Crespo da Silva and Glynn, 1978a, b), who obtained the equations of motion of beams based on inextensibility assumption; they accounted for both geometric and inertial nonlinearities and employed the method of multiple scales to study the cantilever response. Soon after, they (Crespo da Silva and Glynn, 1979) continued the investigations by studying the effect of asymmetries in the support of cantilevers on the vibrating modes nonlinear resonance coupling. The investigations were continued by Nayfeh and Pai (Nayfeh and Pai, 1989), who studied the nonlinear in-plane and out-of-plane oscillations of a cantilever subject to axial base excitation; they derived the cubic nonlinear equations of motion for transverse and lateral motions taking advantage of the inextensibility condition and solved is via the method of multiple scales. In another effort, Pai and Nayfeh (Pai and Nayfeh, 1990) studied the nonlinear in-plane and out-of-plane vibrations of a cantilever under lateral base excitation using the method of multiple scales. Hsieh et al. (Hsieh et al., 1994) obtained the nonlinear normal modes for large-amplitude response of a cantilever making use of an invariant manifold approach taking into account geometric and inertial nonlinearities; they found that the linear vibration mode shapes of a cantilever are very similar to the nonlinear mode shapes.

The investigations on this topic were continued by Oh and Nayfeh (Oh and Nayfeh, 1996), who performed an experimental investigation on composite cantilever plates under lateral harmonic excitation to study the presence of combination resonances. Hamdan and Dado (Hamdan and Dado, 1997) studied the transverse nonlinear free vibrations of a cantilever carrying a point mass utilising the inextensibility assumption and accounting for longitudinal inertia and nonlinear curvature. More studies on nonlinear vibration of cantilevers under parametric excitation were conducted by Anderson et al. (Anderson et al., 1996) and Arafat et al. (Arafat et al., 1998).

Further investigations on nonlinear dynamics of cantilevers were conducted by Herişanu and Marinca (Herişanu and Marinca, 2010) who derived an analytical approximation for the nonlinear free oscillations of a cantilever in the transverse direction through use the inextensibility assumption. The effect of feedback time delays on the nonlinear control of parametrically excited cantilevers was studied by Alhazza et al. (Alhazza et al., 2008), who used the multiple scales method to examine the time delay effects on the stability of the system. The vibration of a cantilever under base motion in a viscous fluid was examined by Phan et al. (Phan et al., 2013), who modelled the fluid-structure interactions using a hydrodynamic function accounting for the added mass of the fluid.

Furthermore, cantilevers have been widely used for mass sensing and vibration-based energy harvesting applications (Friswell et al., 2012; Ghazavi et al., 2010; Kumar et al., 2011; Leadenham and Erturk, 2015; Liu et al., 2012; Mahmoodi and Jalili, 2007). Cantilevers under piezoelectric actuation were studied, for instance, by Mahmoodi and Jalili (Mahmoodi and Jalili, 2007), who used an inextensible beam model to study the nonlinear oscillations of a piezoelectrically actuated microcantilever. Kumar et al. (Kumar et al., 2011) proposed a

bifurcation-based mass sensing approach, using saddle-node type bifurcations, making use of piezoelectrically actuated microcantilevers. Further investigations have been conducted to study the applications of cantilevers in energy harvesting. Liu et al. (Liu et al., 2012) incorporated a stopper in a piezoelectric energy harvesting cantilever system to widen the frequency bandwidth. Leadenham and Erturk (Leadenham and Erturk, 2015) investigated the nonlinear dynamical characteristics of a cantilever-piezoelectric system for energy harvesting, sensing, and actuation applications. The investigations were continued by Staaf et al. (Staaf et al., 2019), who showed the significance of asymmetry in conjoined cantilevers employing a piezoelectric self-tuning energy harvester.

The major limitation of the inextensible model of the cantilever for transverse/lateral motion, when discretised using a modal decomposition technique, is that it can predict displacements only up to the point when the tip angle magnitude is less than 90°. More specifically, to derive the transverse equation of motion of a cantilever under the inextensibility assumption, the cantilever centreline rotation φ is expressed as $\varphi = \sin^{-1}\left(\partial w/\partial x\right)$, where *w* is the transverse displacement; this expression is then expanded via Taylor's series expansion, under the assumption that the centreline angle varies between $\pm 90°$. This means that the transverse equation of motion of a cantilever, if discretised using modal decomposition techniques, is not capable of predicting the response when the tip angle becomes larger than 90°. In this study, the main reason for deriving the cantilever equation of motion for centreline rotation is to overcome this limitation. However, it should be highlighted again that the cantilever centreline equation of motion works accurately only if all the terms are kept exact.

This study examines, for the first time, the nonlinear primary and parametric resonances of a cantilever subject to coupled base motions undergoing extremely large oscillations. An exact model is proposed based on the cantilever centreline rotation allowing for examining the cantilever response at any amplitude. The word “exact” or “geometrically exact” used throughout the text implies that the all the terms are kept intact/exact in the derivation procedure as well as in the discretisation procedure and numerical simulations. The proposed model’s accuracy is verified via comparison to a nonlinear finite element model for a static case. The nonlinear dynamic response of the cantilever in primary and parametric resonance regions due to coupled base motions is examined.

2. Centreline-rotation-based exact cantilever model

An exact cantilever model is developed in this section while treating the centreline rotation as the independent motion of the system. To this end, the beam theory of Euler-Bernoulli is utilised while assuming the centreline remains inextensible. The inertial and curvilinear coordinate systems are shown by *XZ* and *xz* in Fig. 1. One important outcome of the assumption of inextensibility of centreline is that the strain in an element of the centreline remains zero after deformation, i.e. the length of an element before deformation (d*X*) is the same as that after deformation (d*x*). As depicted in Fig. 1, the cantilever is under coupled base excitation. More specifically, a base excitation of $u_0\sin(\omega_0 t)$ is exerted in the axial direction, *X*, while another base excitation of $w_0\sin(\omega_0 t)$ is applied in the transverse direction, *Z*. It is assumed that both base excitations have the same frequency ω_0, but different amplitudes u_0 and w_0.

The exact equation of motion of the centreline rotation of the cantilever is obtained analytically in the following. As explained in the introduction section, the main advantage of deriving the equation of motion for centreline rotation rather than the transverse displacement is in its capability in predicting the cantilever response when the tip angle grows larger than 90°. To this end, the strain energy, motion energy, and Kelvin-Voigt internal damping work are formulated and then inserted into Hamilton's principle.

Utilising the inextensibility assumption, the only strain component developed in the beam axial direction is obtained as

$$\varepsilon\left(t,x,z\right)=-z\frac{\partial}{\partial x}\varphi(t,x), \tag{1}$$

in which φ denotes the centreline rotation angle and t represents time. Based on such axial strain formulation and employing Kelvin-Voigt material damping model, the stress developed in the beam is derived as

$$\sigma\left(t,x,z\right)=-Ez\frac{\partial}{\partial x}\varphi(t,x)-\eta z\frac{\partial^2}{\partial t\partial x}\varphi(t,x), \tag{2}$$

in which η and E represent the material viscosity and Young's modulus, respectively. Hence, the variation of the elastic strain energy of the cantilever can be formulated as

$$\delta\Pi=\int_0^L EI\frac{\partial}{\partial x}\left(\delta\varphi(t,x)\right)\left[\frac{\partial\varphi(t,x)}{\partial x}\right]\mathrm{d}x, \tag{3}$$

in which only the elastic part of the axial stress is included; δ denotes the variational operator, L stands for the length of the cantilever, and I represents the second moment of the beam cross-sectional area.

The internal energy dissipation source is the viscous part of the axial stress; the virtual work of this dissipative source is given by

$$\delta W_{vis} = -\int_0^L \eta I \frac{\partial}{\partial x}\left(\delta\varphi(t,x)\right)\left[\frac{\partial^2\varphi(t,x)}{\partial x \partial t}\right]\mathrm{d}x. \tag{4}$$

In order to derive the kinetic energy formulation in terms of the centreline rotation and base motions, the transverse displacement relative to the base, $w(t,x)$, and the axial displacement relative to the base, $u(t,x)$, must be formulated in terms of the centreline rotation. The centreline inextensibility gives

$$\begin{aligned} w(t,x) &= \int_0^x \sin\left[\varphi(t,s)\right]\mathrm{d}s, \\ u(t,x) &= \int_0^x \left(\cos\left[\varphi(t,s)\right]-1\right)\mathrm{d}s. \end{aligned} \tag{5}$$

Using Eq. (5) and accounting for base motions, the kinetic energy of the cantilever is derived as

$$\begin{aligned} KE = {} & \frac{1}{2}\int_0^L \rho I\left(\frac{\partial\varphi(t,x)}{\partial t}\right)^2 \mathrm{d}x \\ & + \frac{1}{2}\int_0^L \left(\left(M\delta_R\left(x-L\right)+\rho A\right)\left[u_0\omega_0\cos\left(\omega_0 t\right) - \int_0^x \frac{\partial\varphi(t,s)}{\partial t}\sin\left(\varphi(t,s)\right)\mathrm{d}s\right]^2\right)\mathrm{d}x \\ & + \frac{1}{2}\int_0^L \left(\left(M\delta_R\left(x-L\right)+\rho A\right)\left[w_0\omega_0\cos\left(\omega_0 t\right) + \int_0^x \frac{\partial\varphi(t,s)}{\partial t}\cos\left(\varphi(t,s)\right)\mathrm{d}s\right]^2\right)\mathrm{d}x, \end{aligned} \tag{6}$$

in which ρ, A, and M represent the mass density, area of the cross-section, and tip mass, respectively; additionally, δ_R stands for the Dirac delta function.

The exact equation of motion for cantilever centreline rotation can then be derived utilising generalised Hamilton's principle as

$$\cos\varphi\int_L^x\left(\left(M\delta_R\left(x-L\right)+\rho A\right)\left\{w_0\omega_0^2\sin\left(\omega_0 t\right)+\int_0^x\left[-\frac{\partial^2\varphi}{\partial t^2}\cos\varphi+\left(\frac{\partial\varphi}{\partial t}\right)^2\sin\varphi\right]\mathrm{d}x\right\}\right)\mathrm{d}x$$
$$-\sin\varphi\int_L^x\left(M\delta_R\left(x-L\right)+\rho A\right)\left\{u_0\omega_0^2\sin\left(\omega_0 t\right)+\int_0^x\left[\frac{\partial^2\varphi}{\partial t^2}\sin\varphi+\left(\frac{\partial\varphi}{\partial t}\right)^2\cos\varphi\right]\mathrm{d}x\right\}\mathrm{d}x \tag{7}$$
$$+\rho I\frac{\partial^2\varphi}{\partial t^2}-\eta I\frac{\partial^3\varphi}{\partial x^2\partial t}-EI\frac{\partial^2\varphi}{\partial x^2}=0.$$

The dimensionless form of the equation of motion can be obtained as

$$\cos\varphi\int_1^{x_d}\left(\left(\chi\delta_R\left(x_d-1\right)+1\right)\left\{W_0\Omega_0^2\sin\left(\Omega_0\tau\right)+\int_0^{x_d}\left[-\frac{\partial^2\varphi}{\partial\tau^2}\cos\varphi+\left(\frac{\partial\varphi}{\partial\tau}\right)^2\sin\varphi\right]\mathrm{d}x_d\right\}\right)\mathrm{d}x_d$$
$$-\sin\varphi\int_1^{x_d}\left(\chi\delta_R\left(x_d-1\right)+1\right)\left\{U_0\Omega_0^2\sin\left(\Omega_0\tau\right)+\int_0^{x_d}\left[\frac{\partial^2\varphi}{\partial\tau^2}\sin\varphi+\left(\frac{\partial\varphi}{\partial\tau}\right)^2\cos\varphi\right]\mathrm{d}x_d\right\}\mathrm{d}x_d \tag{8}$$
$$+\frac{1}{\beta}\frac{\partial^2\varphi}{\partial\tau^2}-\eta_d\frac{\partial^3\varphi}{\partial x_d^2\partial\tau}-\frac{\partial^2\varphi}{\partial x_d^2}=0,$$

in which the following dimensionless quantities are used

$$\tau=\frac{t}{T},\qquad \Omega_0=\omega_0 T,\qquad \eta_d=\frac{\eta}{ET},\qquad x_d=\frac{x}{L},$$
$$\chi=\frac{M}{\rho AL},\qquad U_0=\frac{u_0}{L},\qquad W_0=\frac{w_0}{L},\qquad \beta=\frac{AL^2}{I}, \tag{9}$$

where $T=L^2\sqrt{\rho A/(EI)}$.

The exact equation of centreline rotational motion of the cantilever is obtained in Eq. (8). Being exact, this model is capable of predicting very large-amplitude motions as will be discussed in detail later. To ensure the accuracy of the developed model, it is essential to keep all terms exact while performing the Galerkin discretisation technique. Based on the Galerkin modal decomposition method, the centreline rotation is defined as a finite series expansion consisting of spatial shape functions $\Psi_k(x_d)$ multiplied by generalised

coordinates $r_k(\tau)$. To ensure fast convergence, the following hyperbolic function is used as the shape function

$$\Psi_k(x_d)=\left(\sin\left(\mu_k x_d\right)+\kappa_k\cos\left(\mu_k x_d\right)\right)+\left(\sinh\left(\mu_k x_d\right)-\kappa_k\cosh\left(\mu_k x_d\right)\right),$$
$$\kappa_k=\left(\sinh\left(\mu_k\right)+\sin\left(\mu_k\right)\right)^{-1}\left(\cosh\left(\mu_k\right)+\cos\left(\mu_k\right)\right), \tag{10}$$

where μ_k is the kth root of the equation $\cos(\mu)\cosh(\mu)+1=0$. The hyperbolic function in Eq. (10) is obtained as $\Psi_k(x_d)=\frac{1}{\mu_k}\frac{\partial\Delta(x_d)}{\partial x_d}$, where $\Delta(x_d)$ is the eigenfunction for the transverse motion of a cantilever. The rotational discretised equations of motion of the cantilever can be obtained, via Galerkin's method (Ghayesh et al., 2013a; Kazemirad et al., 2013), as

$$\begin{aligned}
&\int_0^1\Psi_j\left\{\cos\left(\sum_{k=1}^{M}r_k(\tau)\Psi_k(x_d)\right)\int_1^{x_d}\left(\chi\delta_R\left(x_d-1\right)+1\right)\left(\int_0^{x_d}\left[-\frac{\partial^2}{\partial\tau^2}\left(\sum_{k=1}^{M}r_k(\tau)\Psi_k(x_d)\right)\cos\left(\sum_{k=1}^{M}r_k(\tau)\Psi_k(x_d)\right)\right.\right.\right.\\
&\left.\left.\left.+\left(\frac{\partial}{\partial\tau}\left(\sum_{k=1}^{M}r_k(\tau)\Psi_k(x_d)\right)\right)^2\sin\left(\sum_{k=1}^{M}r_k(\tau)\Psi_k(x_d)\right)\right]\mathrm{d}x_d+W_0\Omega_0^2\sin\left(\Omega_0\tau\right)\right)\mathrm{d}x_d\right\}\mathrm{d}x_d\\
&-\int_0^1\Psi_j\left\{\sin\left(\sum_{k=1}^{M}r_k(\tau)\Psi_k(x_d)\right)\int_1^{x_d}\left(\chi\delta_R\left(x_d-1\right)+1\right)\left(\int_0^{x_d}\left[\frac{\partial^2}{\partial\tau^2}\left(\sum_{k=1}^{M}r_k(\tau)\Psi_k(x_d)\right)\sin\left(\sum_{k=1}^{M}r_k(\tau)\Psi_k(x_d)\right)\right.\right.\right.\\
&\left.\left.\left.+\left(\frac{\partial}{\partial\tau}\left(\sum_{k=1}^{M}r_k(\tau)\Psi_k(x_d)\right)\right)^2\cos\left(\sum_{k=1}^{M}r_k(\tau)\Psi_k(x_d)\right)\right]\mathrm{d}x_d+U_0\Omega_0^2\sin\left(\Omega_0\tau\right)\right)\mathrm{d}x_d\right\}\mathrm{d}x_d\\
&+\frac{1}{\beta}\sum_{k=1}^{M}\left(\int_0^1\Psi_j\Psi_k\,\mathrm{d}x_d\right)\ddot{r}_k-\eta_d\sum_{k=1}^{M}\left(\int_0^1\Psi_j\Psi_k''\,\mathrm{d}x_d\right)\dot{r}_k-\sum_{k=1}^{M}\left(\int_0^1\Psi_j\Psi_k''\,\mathrm{d}x_d\right)r_k=0,\\
&j=1,2,\ldots,M.
\end{aligned} \tag{11}$$

It is noted that in Eq. (11), all sin and cos terms are kept intact; this is absolutely necessary to ensure accurate results when the cantilever undergoes extreme deformations. In other words, the sin and cos terms should not be approximated using Taylor's expansion

and must be kept intact to guarantee accurate results. The main challenge encountered while doing so is that the integrations cannot be performed in closed form due to presence of time-dependent terms in the arguments of sin and cos terms. Hence, numerical integration is utilised for these terms while retaining sufficient number of terms to guarantee accurate results. This is a challenging task which yields extremely large-size equations of motion; solving such large equations requires high computational costs. Additionally, to ensure convergence, six generalised coordinates are retained in Galerkin discretisation resulting in six nonlinearly coupled second-order ordinary differential equations. The resultant set of equations is solved via developing well-optimised codes based on a continuation technique. Once the discretised equations are solved, the transverse and axial displacements are calculated using the expressions given in Eq. (5). Apart from the dimensionless quantities defined in Eq. (9), the following dimensionless quantities are used as well in the reported numerical results

$$u_d = \frac{u}{L}, \qquad w_d = \frac{w}{L}, \qquad X_d = \frac{X}{L}, \qquad Z_d = \frac{Z}{L}, \qquad \omega_1 = \bar{\omega}_1 T, \tag{12}$$

in which ω_1 is the first dimensionless transverse natural frequency of the cantilever.

3. Nonlinear large-amplitude static analysis

A nonlinear static investigation is conducted in this section using a cantilever model based on the centreline rotation as well as a three-dimensional (3D) nonlinear finite element (FE) model. A specific tip load configuration is assumed as shown in Fig. 2(a) to force the cantilever to undergo extremely large deformations. The exact model of the cantilever shown in Fig. 2(a) based on the centreline rotation can be derived as

$$p_d\left[\cos\varphi\int_1^{x_d}\left[\delta_R(x_d-1)\left(\sin\varphi+\cos\varphi\right)\right]\mathrm{d}x_d-\sin\varphi\int_1^{x_d}\left[\delta_R(x_d-1)\left(\cos\varphi-\sin\varphi\right)\right]\mathrm{d}x_d\right]$$
$$-\frac{\partial^2\varphi}{\partial x_d^2}=0, \tag{13}$$

in which $p_d=pL^2/(EI)$, where p is the tip load magnitude in both axial and transverse directions as shown in Fig. 2(a). Equation (13) is discretised using the same procedure defined in Section 2, retaining 6 vibration modes. A 3D nonlinear FE model is developed as well through use of Abaqus employing continuum shell elements, i.e. an 8-node quadrilateral element with reduced integration. A mesh size of 1 mm is used to ensure converged results. For this comparison, a cantilever of length 140 mm, thickness 0.8 mm, and width 4 mm is used for both models.

The nonlinear extremely large static deflection of the cantilever under various tip load magnitudes is illustrated in Fig. 2(b); the results obtained via the proposed exact model are shown by solid lines while the FE results are indicated by solid circles. It is interesting to note that the proposed centreline-rotation-based cantilever model predicts almost the same responses as the nonlinear 3D FE model even at extreme deformations. In fact, for the case with p_d=9.0, the tip of the cantilever has completely bent backwards, and yet the proposed model has no problem in capturing the response accurately. This comparison shows the robustness and reliability of the proposed exact model in predicting the cantilever response even at extreme deformations. Figure 3 shows the cantilever deformed configurations obtained via the nonlinear FE model for p_d=3.0, 5.0, and 9.0 through sub-figures (a)-(c), respectively; the contour plots show the transverse displacement in mm.

4. Primary and parametric resonances due to coupled based motions

Extensive numerical simulations are conducted in this section in order to examine the nonlinear primary and parametric resonances of the cantilever subject to coupled axial-transverse base motions. All the results presented in this section are dimensionless so that they can be used for benchmark analysis. The dimensionless material viscosity η_d is set to 0.003 for all the cases examined in this section. The only parameter whose value requires defining dimensional parameters is β. Recalling from Section 2, $\beta=AL^2/I$, which for a rectangular cross section of thickness h reduces to $12(L/h)^2$. In other words, the value of β depends on the slenderness ratio of the beam. In this study, β is set to 120000, corresponding to L/h =100; however, for cantilevers with L/h>50, β has a negligible effect on resonance response since it will be large enough so that the term $1/\beta$ will be negligible. In all the frequency-amplitude diagrams presented in this section, the line style indicates the stability with the solid style representing stable response and the dashed style showing the unstable one. The word “stability” in this study implies “structural stability” which refers to the effect of small perturbations on the behaviour of the dynamical system trajectories.

In what follows, the primary and parametric resonance responses of the cantilever are studied in detail. The transverse base motion is responsible for the primary resonance response while the axial base motion is responsible for emergence of another resonance region in the vicinity of twice the first natural frequency, namely the parametric resonance region. Figure 4 shows the resonance responses of the cantilever under coupled base motions of the same amplitudes; more specifically, $W_0=U_0=0.012$. At first glance, it is seen that the cantilever undergoes very large-amplitude oscillations with transverse amplitudes reaching almost 90% of the length and the tip angle reaching almost 180 degrees; these

extreme amplitudes are discussed in more detail later. It is interesting to note that although the base motion amplitude is the same in both axial and transverse directions, the parametric resonance oscillation amplitudes are much larger than those in the primary resonance region, mainly due to larger frequency of excitation. Figure 4(a) shows the maximum transverse displacement of the cantilever; as seen in this figure, as the excitation frequency is increased from values smaller than ω_1, the oscillation amplitude increases gradually with increasing frequency in the primary resonance region until reaching a peak amplitude. At this point (Ω_0/ω_1=1.0256), a saddle-node type bifurcation occurs and the cantilever jumps to a smaller-amplitude branch. In fact, there are two saddle-node bifurcations in the primary resonance region, with the second one occurring at Ω_0/ω_1=1.01908. Then, in the vicinity of $2\omega_1$, two period-doubling bifurcations occur at Ω_0/ω_1= 1.9640 and 2.0364, rendering the trivial solution branch unstable and giving rise to two nontrivial solution branches, one being stable and the other one unstable. The two motion branches coincide at the point shown on the curve in which yet another saddle-point bifurcation occurs (Ω_0/ω_1= 2.0824). Figure 4(b) shows the tip transverse displacement corresponding to maximum tip rotation. The goal of this figure is to better highlight extreme oscillations of the cantilever when the tip of the cantilever bends backwards. As seen in Fig. 4(b), the tip *w* motion corresponding to maximum tip rotation in the parametric resonance region reaches a maximum and the decreases with increasing frequency. In fact, the maximum value corresponds to a tip rotation of 106°; this means that for larger tip angles, the transverse amplitude of the tip of the cantilever first reaches a maximum and then decreases as the cantilever reaches its limiting states. This is better illustrated in Fig. 5, through plotting the oscillation of the cantilever in (a) peak amplitude of primary resonance and (b) peak amplitude of parametric resonance. As seen in Fig. 5(b), the cantilever tip

bends completely backward during the oscillation. Such an extreme response can only be captured using the exact model developed in this study. To better show the vibration characteristics of the system, Figs. 6 and 7 are constructed showing the phase-plane plots and time traces of the transverse, rotational, and axial motions at Ω_0/ω_1=1.0256 and 2.0779, respectively. A closer look at Fig. 7(b) and (d) shows that the tip transverse displacement reaches a local minimum as the tip rotation reaches its maximum during one period of oscillation.

Figure 8 shows the frequency-amplitude curves of the cantilever in primary and parametric resonance regions for various base motion amplitudes; the base motion amplitude is denoted on the curves noting that W_0=U_0 for all cases. It is interesting to note that a primary resonance region appear for all four cases while the parametric resonance region appear only for three base motion amplitudes. More specifically, for the case with base motion amplitude of 0.003, no parametric resonance occurs. Hence, although when W_0=U_0 the parametric resonance amplitude is larger than the primary resonance one, at small enough base motion amplitudes, no parametric resonance appears.

The effect of the parameter χ, i.e. the tip mass ratio, on resonance responses of the cantilever when W_0=U_0=0.009 is depicted in Fig. 9. As seen in sub-figure (c) and (d), as the tip mass ratio is increased, the peak tip rotation and axial displacement increases accordingly; however, the tip maximum transverse displacement is not affected much by increasing tip mass ratio, as seen in Fig. 9(a). Additionally, it is seen that due to increased tip mass ratio, both resonance regions shift to smaller base motion frequencies. As seen, the shift in the parametric resonance region is more pronounced compared to the primary resonance region. The figure also shows that the shift in the frequency becomes less as the

tip mass ratio increases; more specifically, a larger shift is seen as χ is increased from 0 to 0.04 compared to the case when it is increased from 0.12 to 0.16.

For the next case, i.e. Fig. 10, the axial base motion amplitude, U_0, is set to 0.007 while the transverse base motion amplitude, W_0, is set to 0.028, i.e. $W_0=4U_0$. As seen in Fig. 10, setting $W_0=4U_0$ results in very similar peak oscillation amplitudes in primary and parametric resonance regions, with two saddle-node bifurcations appearing in the primary resonance region at Ω_0/ω_1=1.0351 and 1.0307 and another one in the parametric resonance region Ω_0/ω_1=2.0686; the period-doubling bifurcations occur at Ω_0/ω_1= 1.9759 and 2.0144. The cantilever behaviour in the two regions, on the other hand, is very different. The primary resonance region is very wide and the increase in the amplitude is gradual while the parametric resonance region is very narrow and the increase in the amplitude is very sharp. The number of saddle-node and period-doubling bifurcation points remain unchanged compared to the case of Fig. 4. The oscillations of the cantilever at peak primary and parametric resonances are shown in Fig. 11.

The effect the tip mass ratio on resonance responses of the cantilever when W_0=0.020 and U_0=0.006 is illustrated in Fig. 12. As seen, the added tip mass effect is similar to the case of Fig. 10; however, in this case due to larger amplitude of the base motion in the transverse direction, the primary and secondary resonance responses are of similar amplitudes.

5. Conclusions

In this study, an exact model was developed for the centreline rotation of a cantilever under coupled axial-transverse base motions. More specifically, the equation of motion of the cantilever was derived for the centreline rotation assuming inextensibility condition and all the terms were kept intact in the derivation procedure. The Galerkin technique was used to discretise the equation of motion using hyperbolic shape functions for fast convergence; all terms were kept exact in discretisation process.

First, a nonlinear static analysis was conducted to examine extremely large deformations of the cantilever. The results obtained via the proposed model were compared to those of 3D nonlinear FE analysis, showing excellent agreement between the two. The verified exact cantilever model was then utilised to study the resonance response of a cantilever subject to coupled axial-transverse base motions. The frequency-amplitude diagram showed that the cantilever displays a primary resonance response as well as a parametric one when the excitation frequency is twice the fundamental transverse natural frequency. The exact cantilever model predicted a weakly hardening nonlinear behaviour in both primary and parametric resonance regions. The results showed that the cantilever could undergo vibrations of extreme amplitude with the tip angle growing larger than 180°, i.e. with the tip bending completely backward.

Examining the effect of base motion amplitudes revealed that the parametric resonance region exists only when the axial base motion amplitude is sufficiently large. It was shown when the axial and transverse base motion amplitudes are the same, the peak oscillation amplitude in parametric resonance region is much larger than that in the primary resonance region. Examining the effect of an added tip mass on resonance response

characteristics of the cantilever showed that a shift to smaller base motion frequencies occurs in both primary and parametric resonance regions. It was shown that the shift in the frequency becomes smaller at larger tip mass ratios.

References

AkhavanAlavi, S.M., Mohammadimehr, M., Edjtahed, S.H., 2019. Active control of micro Reddy beam integrated with functionally graded nanocomposite sensor and actuator based on linear quadratic regulator method. European Journal of Mechanics, A/Solids 74, 449-461.

Alhazza, K.A., Daqaq, M.F., Nayfeh, A.H., Inman, D.J., 2008. Non-linear vibrations of parametrically excited cantilever beams subjected to non-linear delayed-feedback control. International Journal of Non-Linear Mechanics 43, 801-812.

Anderson, T., Nayfeh, A., Balachandran, B., 1996. Experimental verification of the importance of the nonlinear curvature in the response of a cantilever beam. Journal of Vibration and Acoustics 118, 21-27.

Arafat, H.N., Nayfeh, A.H., Chin, C.-M., 1998. Nonlinear nonplanar dynamics of parametrically excited cantilever beams. Nonlinear Dynamics 15, 31-61.

Ashoori Movassagh, A., Mahmoodi, M.J., 2013. A micro-scale modeling of Kirchhoff plate based on modified strain-gradient elasticity theory. European Journal of Mechanics - A/Solids 40, 50-59.

Basutkar, R., Sidhardh, S., Ray, M.C., 2019. Static analysis of flexoelectric nanobeams incorporating surface effects using element free Galerkin method. European Journal of Mechanics, A/Solids 76, 13-24.

Crespo da Silva, M., Glynn, C., 1978a. Nonlinear flexural-flexural-torsional dynamics of inextensional beams. I. Equations of motion. Journal of Structural Mechanics 6, 437-448.

Crespo da Silva, M., Glynn, C., 1978b. Nonlinear flexural-flexural-torsional dynamics of inextensional beams. II. Forced motions. Journal of Structural Mechanics 6, 449-461.

Crespo da Silva, M., Glynn, C., 1979. Non-linear non-planar resonant oscillations in fixed-free beams with support asymmetry. International Journal of Solids and Structures 15, 209-219.

Farokhi, H., Ghayesh, M., Amabili, M., 2013. Nonlinear dynamics of a geometrically imperfect microbeam based on the modified couple stress theory. International Journal of Engineering Science 68 11-23.

Friswell, M.I., Ali, S.F., Bilgen, O., Adhikari, S., Lees, A.W., Litak, G., 2012. Non-linear piezoelectric vibration energy harvesting from a vertical cantilever beam with tip mass. Journal of Intelligent Material Systems and Structures 23, 1505-1521.

Ghayesh, M., 2012. Subharmonic dynamics of an axially accelerating beam. Archive of Applied Mechanics 82, 1169-1181.

Ghayesh, M., Moradian, N., 2011. Nonlinear dynamic response of axially moving, stretched viscoelastic strings. Archive of Applied Mechanics 81, 781-799.

Ghayesh, M.H., Amabili, M., Farokhi, H., 2013a. Coupled global dynamics of an axially moving viscoelastic beam. International Journal of Non-Linear Mechanics 51, 54-74.

Ghayesh, M.H., Amabili, M., Farokhi, H., 2013b. Three-dimensional nonlinear size-dependent behaviour of Timoshenko microbeams. International Journal of Engineering Science 71, 1-14.

Ghayesh, M.H., Farokhi, H., 2015a. Chaotic motion of a parametrically excited microbeam. International Journal of Engineering Science 96, 34-45.

Ghayesh, M.H., Farokhi, H., 2015b. Nonlinear dynamics of microplates. International Journal of Engineering Science 86, 60-73.

Ghayesh, M.H., Farokhi, H., Alici, G., 2016. Size-dependent performance of microgyroscopes. International Journal of Engineering Science 100, 99-111.

Ghayesh, M.H., Farokhi, H., Amabili, M., 2013c. Nonlinear dynamics of a microscale beam based on the modified couple stress theory. Composites Part B: Engineering 50, 318-324.

Ghayesh, M.H., Farokhi, H., Amabili, M., 2014. In-plane and out-of-plane motion characteristics of microbeams with modal interactions. Composites Part B: Engineering 60, 423-439.

Ghayesh, M.H., Farokhi, H., Gholipour, A., 2017. Coupled vibrations of functionally graded Timoshenko microbeams. European Journal of Mechanics - A/Solids 65, 289-300.

Ghayesh, M.H., Yourdkhani, M., Balar, S., Reid, T., 2010. Vibrations and stability of axially traveling laminated beams. Applied Mathematics and Computation 217, 545-556.

Ghazavi, M.-R., Rezazadeh, G., Azizi, S., 2010. Pure parametric excitation of a micro cantilever beam actuated by piezoelectric layers. Applied Mathematical Modelling 34, 4196-4207.

Gholipour, A., Farokhi, H., Ghayesh, M.H., 2015. In-plane and out-of-plane nonlinear size-dependent dynamics of microplates. Nonlinear Dynamics 79, 1771-1785.

Gusella, F., Cluni, F., Gusella, V., 2019. Homogenization of dynamic behaviour of heterogeneous beams with random Young's modulus. European Journal of Mechanics, A/Solids 73, 260-267.

Hamdan, M., Dado, M., 1997. Large amplitude free vibrations of a uniform cantilever beam carrying an intermediate lumped mass and rotary inertia. Journal of Sound and Vibration 206, 151-168.

Herişanu, N., Marinca, V., 2010. Explicit analytical approximation to large-amplitude non-linear oscillations of a uniform cantilever beam carrying an intermediate lumped mass and rotary inertia. Meccanica 45, 847-855.

Hsieh, S.-R., Shaw, S.W., Pierre, C., 1994. Normal modes for large amplitude vibration of a cantilever beam. International Journal of Solids and Structures 31, 1981-2014.

Karimi, H.R., 2006. Optimal vibration control of vehicle engine-body system using Haar functions. International Journal of Control, Automation and Systems 4, 714-724.

Kazemirad, S., Ghayesh, M., Amabili, M., 2013. Thermo-mechanical nonlinear dynamics of a buckled axially moving beam. Archive of Applied Mechanics 83, 25-42.

Kumar, V., Boley, J.W., Yang, Y., Ekowaluyo, H., Miller, J.K., Chiu, G.T.-C., Rhoads, J.F., 2011. Bifurcation-based mass sensing using piezoelectrically-actuated microcantilevers. Applied Physics Letters 98, 153510.

Leadenham, S., Erturk, A., 2015. Unified nonlinear electroelastic dynamics of a bimorph piezoelectric cantilever for energy harvesting, sensing, and actuation. Nonlinear Dynamics 79, 1727-1743.

Li, G., de Miguel, A.G., Pagani, A., Zappino, E., Carrera, E., 2019. Finite beam elements based on Legendre polynomial expansions and node-dependent kinematics for the global-local analysis of composite structures. European Journal of Mechanics, A/Solids 74, 112-123.

Liu, H., Lee, C., Kobayashi, T., Tay, C.J., Quan, C., 2012. Piezoelectric MEMS-based wideband energy harvesting systems using a frequency-up-conversion cantilever stopper. Sensors and Actuators A: Physical 186, 242-248.

Mahmoodi, S.N., Jalili, N., 2007. Non-linear vibrations and frequency response analysis of piezoelectrically driven microcantilevers. International Journal of Non-Linear Mechanics 42, 577-587.

Mirsalehi, M., Azhari, M., Amoushahi, H., 2017. Buckling and free vibration of the FGM thin micro-plate based on the modified strain gradient theory and the spline finite strip method. European Journal of Mechanics - A/Solids 61, 1-13.

Mitchell, D., Gau, J.T., 2019. Exact analytical solution to the 3D Navier-Lame equation for a curved beam of constant curvature subject to arbitrary dynamic loading. European Journal of Mechanics, A/Solids 75, 216-224.

Nampally, P., Karttunen, A.T., Reddy, J.N., 2019. Nonlinear finite element analysis of lattice core sandwich beams. European Journal of Mechanics, A/Solids 74, 431-439.

Nayfeh, A.H., Pai, P.F., 1989. Non-linear non-planar parametric responses of an inextensional beam. International Journal of Non-Linear Mechanics 24, 139-158.

Oh, K., Nayfeh, A.H., 1996. Nonlinear combination resonances in cantilever composite plates. Nonlinear Dynamics 11, 143-169.

Pai, P.F., Nayfeh, A.H., 1990. Non-linear non-planar oscillations of a cantilever beam under lateral base excitations. International Journal of Non-Linear Mechanics 25, 455-474.

Palacios-Quiñonero, F., Rubió-Massegú, J., Rossell, J.M., Karimi, H.R., 2012. Semiactive–passive structural vibration control strategy for adjacent structures under seismic excitation. Journal of the Franklin Institute 349, 3003-3026.

Phan, C.N., Aureli, M., Porfiri, M., 2013. Finite amplitude vibrations of cantilevers of rectangular cross sections in viscous fluids. Journal of Fluids and Structures 40, 52-69.

Reddy, J.N., Romanoff, J., Loya, J.A., 2016. Nonlinear finite element analysis of functionally graded circular plates with modified couple stress theory. European Journal of Mechanics, A/Solids 56, 92-104.

Rokni, H., Milani, A.S., Seethaler, R.J., 2015. Size-dependent vibration behavior of functionally graded CNT-Reinforced polymer microcantilevers: Modeling and optimization. European Journal of Mechanics, A/Solids 49, 26-34.

Ruzziconi, L., Bataineh, A.M., Younis, M.I., Cui, W., Lenci, S., 2013. Nonlinear dynamics of an electrically actuated imperfect microbeam resonator: experimental investigation and reduced-order modeling. Journal of Micromechanics and Microengineering 23, 075012.

Sadeghmanesh, M., Haddadpour, H., Abadi, M.T., Navazi, H.M., 2019. A method for selection of structural theories for low to high frequency vibration analyses. European Journal of Mechanics, A/Solids 75, 27-40.

Si, Y., Karimi, H.R., Gao, H., 2014. Modelling and optimization of a passive structural control design for a spar-type floating wind turbine. Engineering Structures 69, 168-182.

Staaf, L.G.H., Smith, A.D., Lundgren, P., Folkow, P.D., Enoksson, P., 2019. Effective piezoelectric energy harvesting with bandwidth enhancement by assymetry augmented self-tuning of conjoined cantilevers. International Journal of Mechanical Sciences 150, 1-11.

Talimian, A., Béda, P., 2018. Dynamic stability of a size-dependent micro-beam. European Journal of Mechanics - A/Solids 72, 245-251.

Wang, B., Zhou, S., Zhao, J., Chen, X., 2011. A size-dependent Kirchhoff micro-plate model based on strain gradient elasticity theory. European Journal of Mechanics - A/Solids 30, 517-524.

Xu, X.J., Deng, Z.C., 2016. Closed-form frequency solutions for simplified strain gradient beams with higher-order inertia. European Journal of Mechanics, A/Solids 56, 59-72.

Zhang, B., He, Y., Liu, D., Gan, Z., Shen, L., 2013. A non-classical Mindlin plate finite element based on a modified couple stress theory. European Journal of Mechanics - A/Solids 42, 63-80.

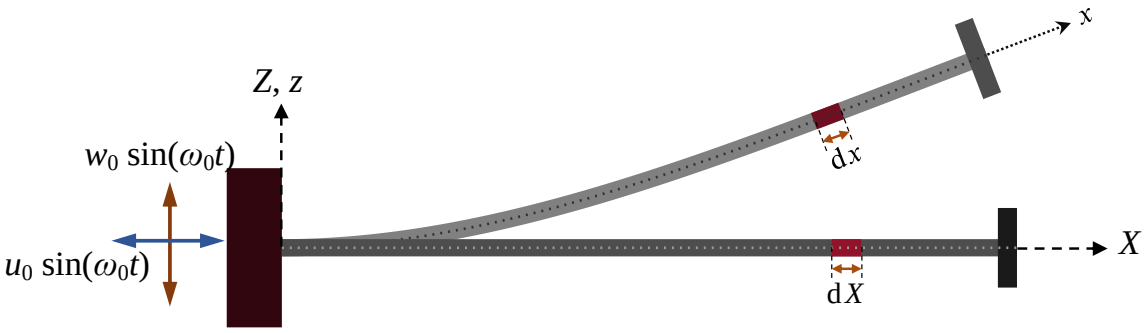

Fig. 1. Schematic of a cantilever with a tip mass subject to coupled axial-transverse base motions.

(a)

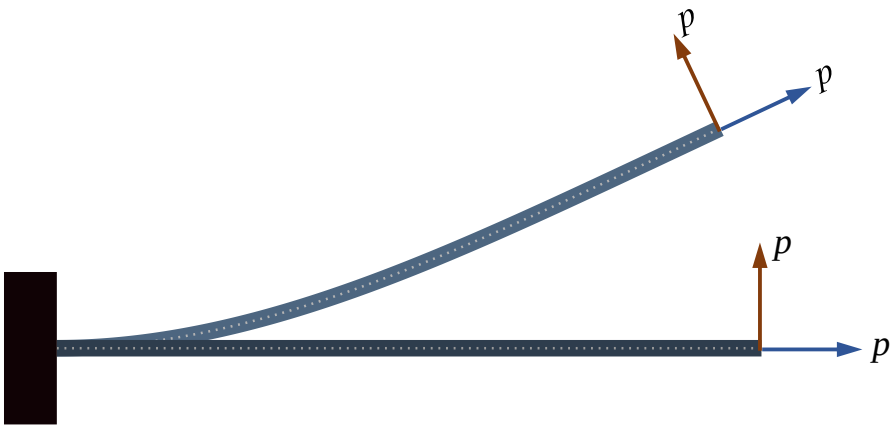

(b)

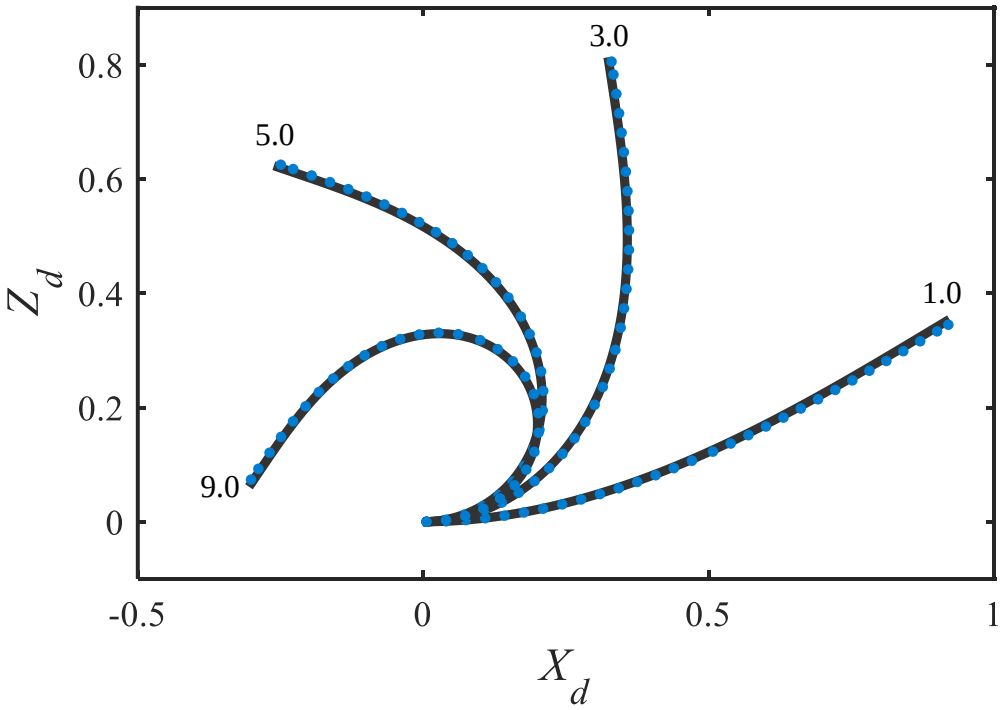

Fig.2. (a) Cantilever under static tip load; (b) extreme static deformations of the cantilever under various tip loads (values of p_d denoted on the diagrams); solid line shows the results obtained by the proposed exact model while solid circles show those calculated via 3D nonlinear FE analysis.

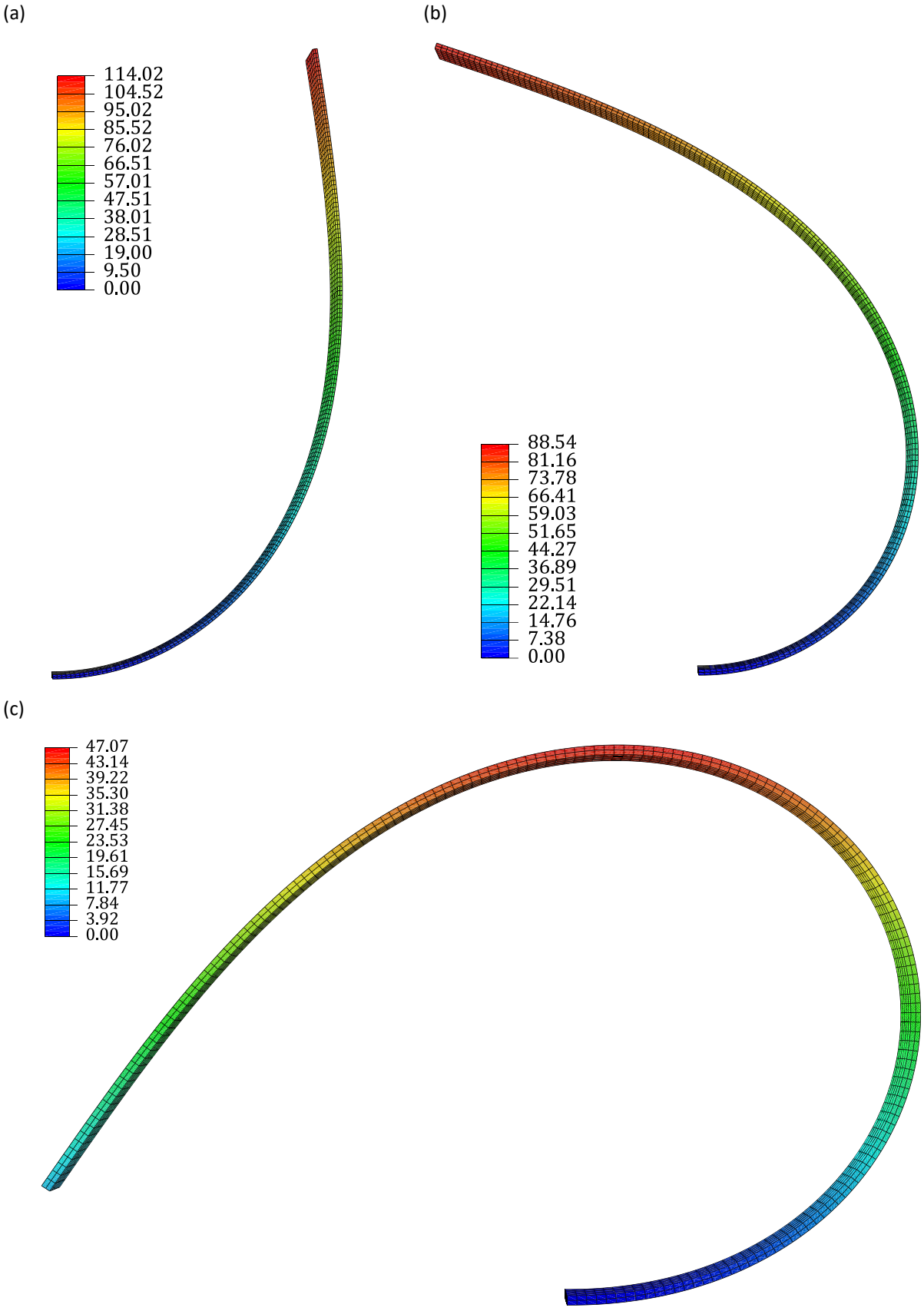

Fig. 3. Transverse displacement contour plots of the cantilever of Fig. 3 (in mm) for (a-c) p_d = 3.0, 5.0, and 9.0, respectively.

(a)

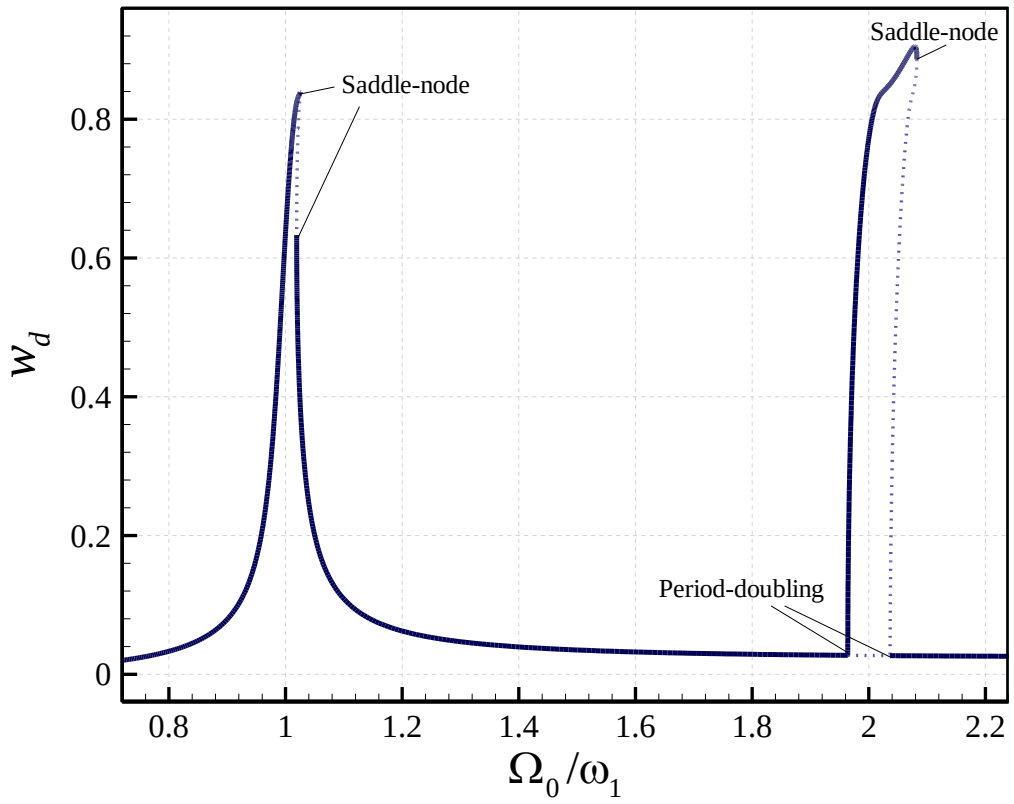
Saddle-node
Saddle-node
Period-doubling
w_d
Ω_0/ω_1
0
0.2
0.4
0.6
0.8
0.8
1
1.2
1.4
1.6
1.8
2
2.2

(b)

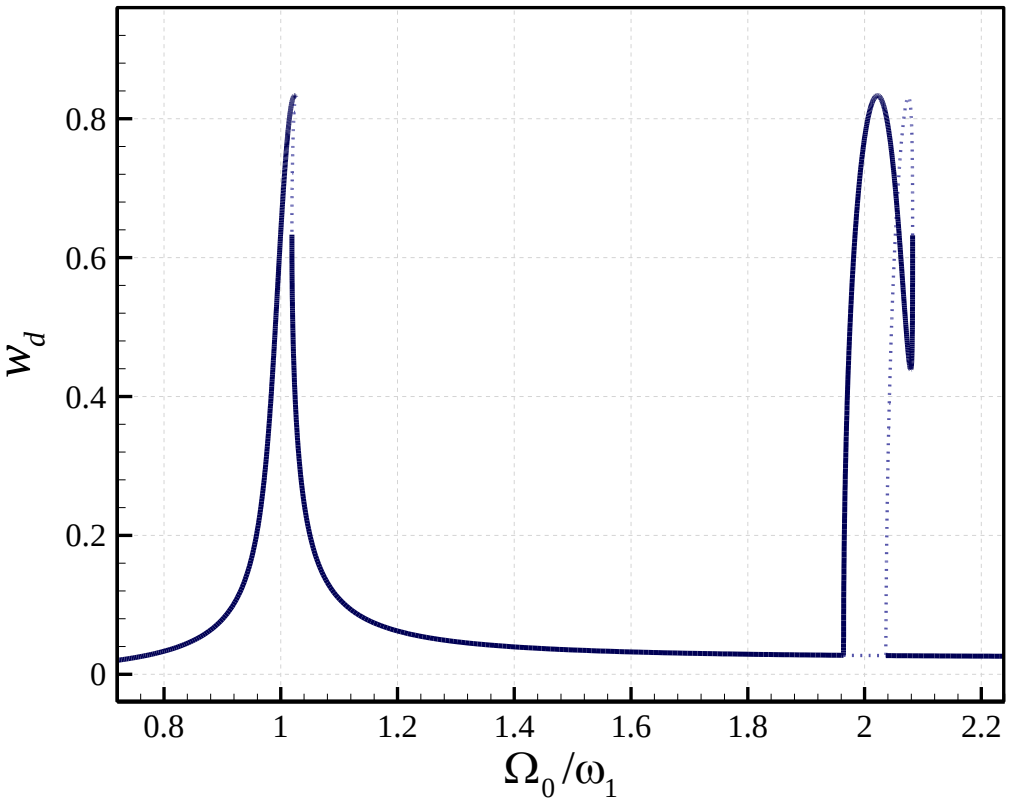
w_d
Ω_0/ω_1
0
0.2
0.4
0.6
0.8
0.8
1
1.2
1.4
1.6
1.8
2
2.2

(c)

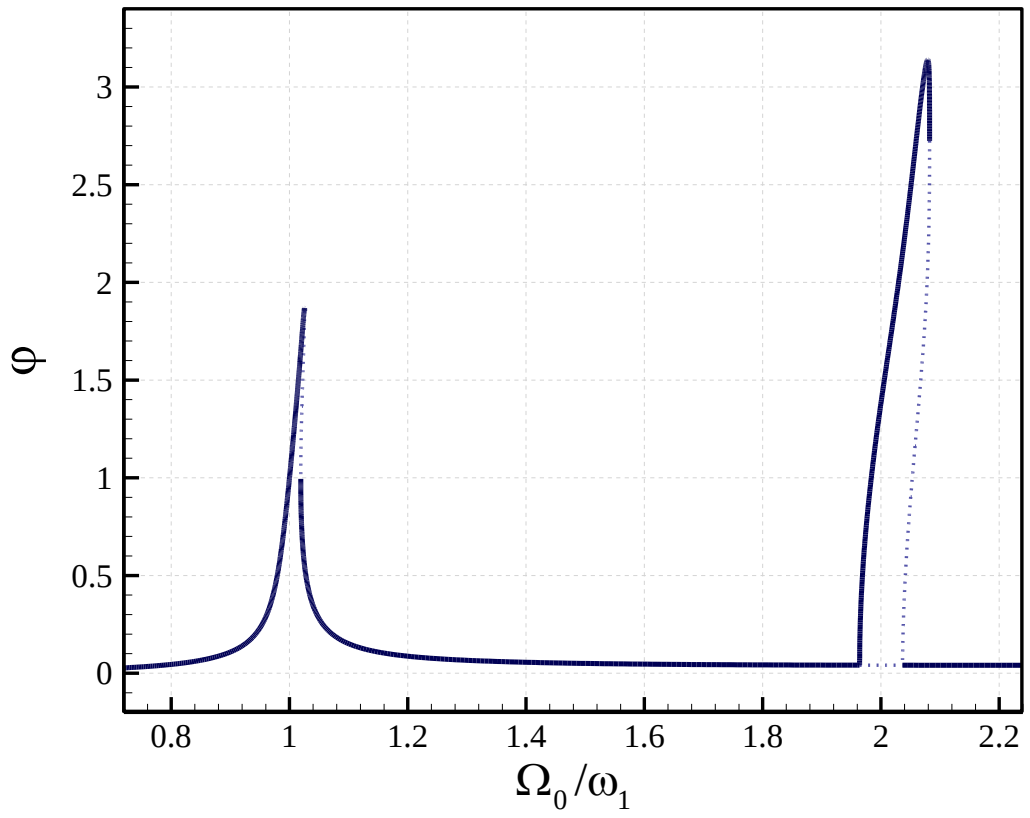

(d)

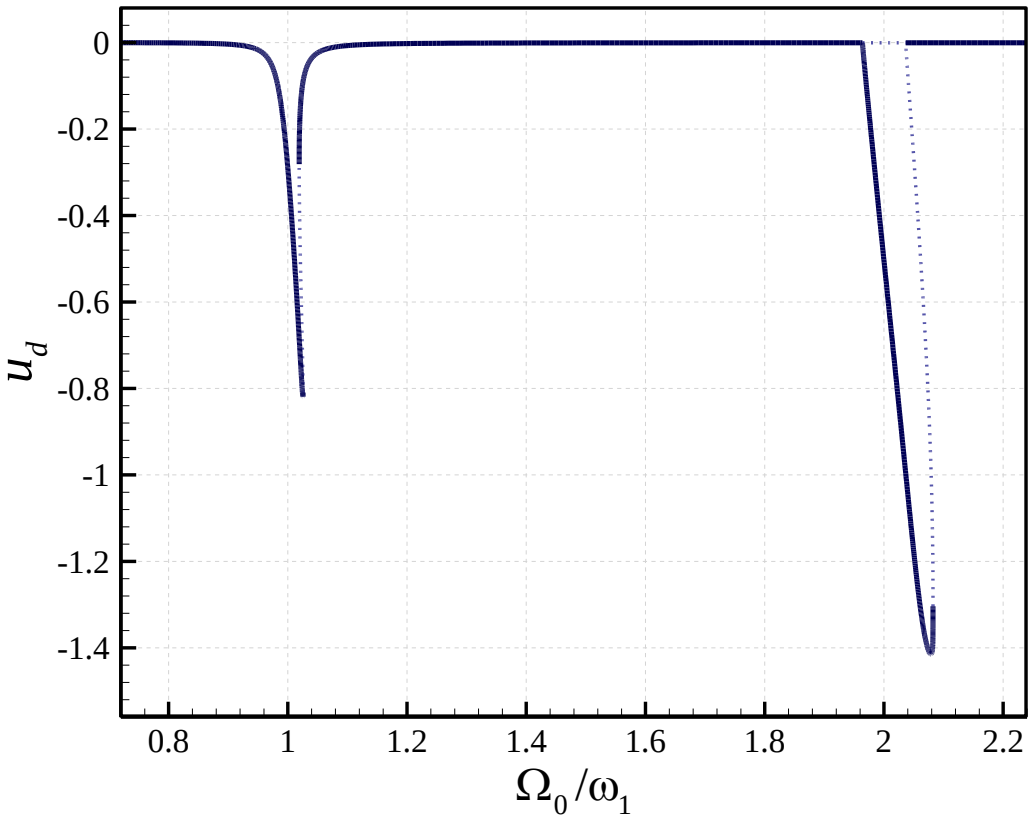

Fig.4. Large-amplitude oscillations of the cantilever under coupled base motions in primary and parametric resonance regions; (a) maximum transverse displacement at tip; (b) tip transverse displacement at the time of maximum tip rotation; (c) maximum rotation at tip; (d) maximum axial displacement at tip. W_0=U_0=0.012.

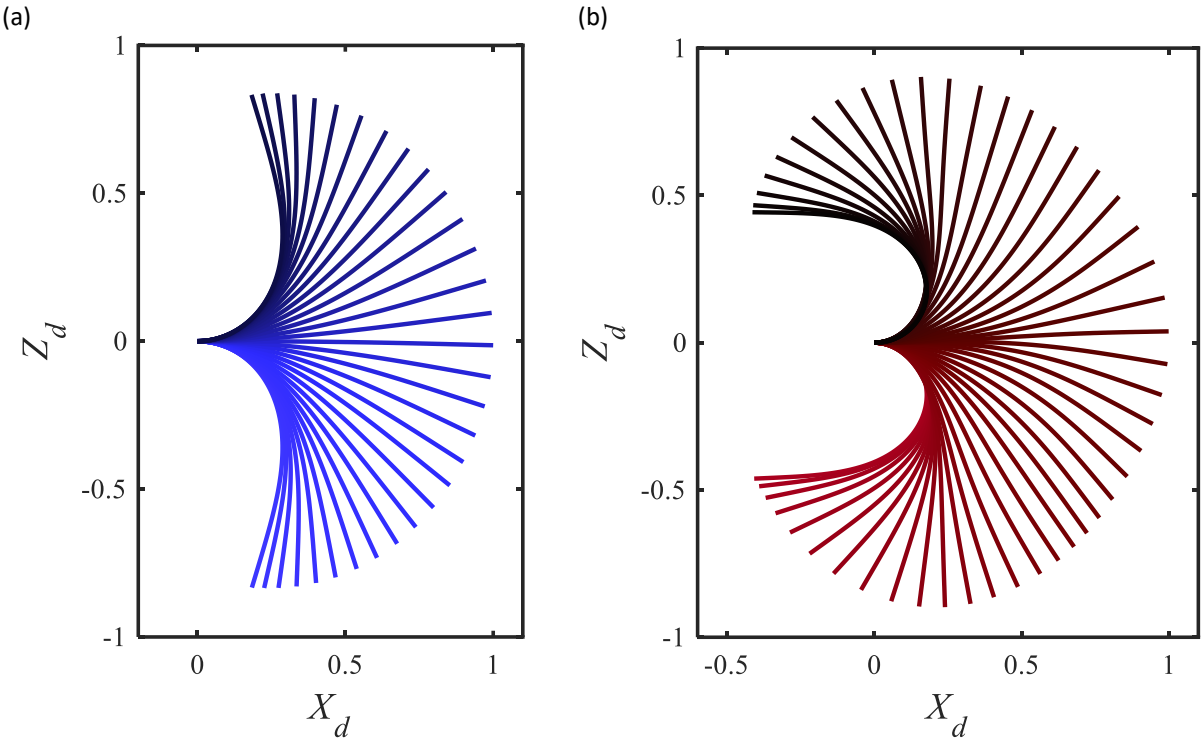

Fig.5. Oscillations of the cantilever of Fig. 4; (a) primary resonance response at Ω_0/ω_1=1.0256 and (b) parametric resonance response at Ω_0/ω_1=2.0779.

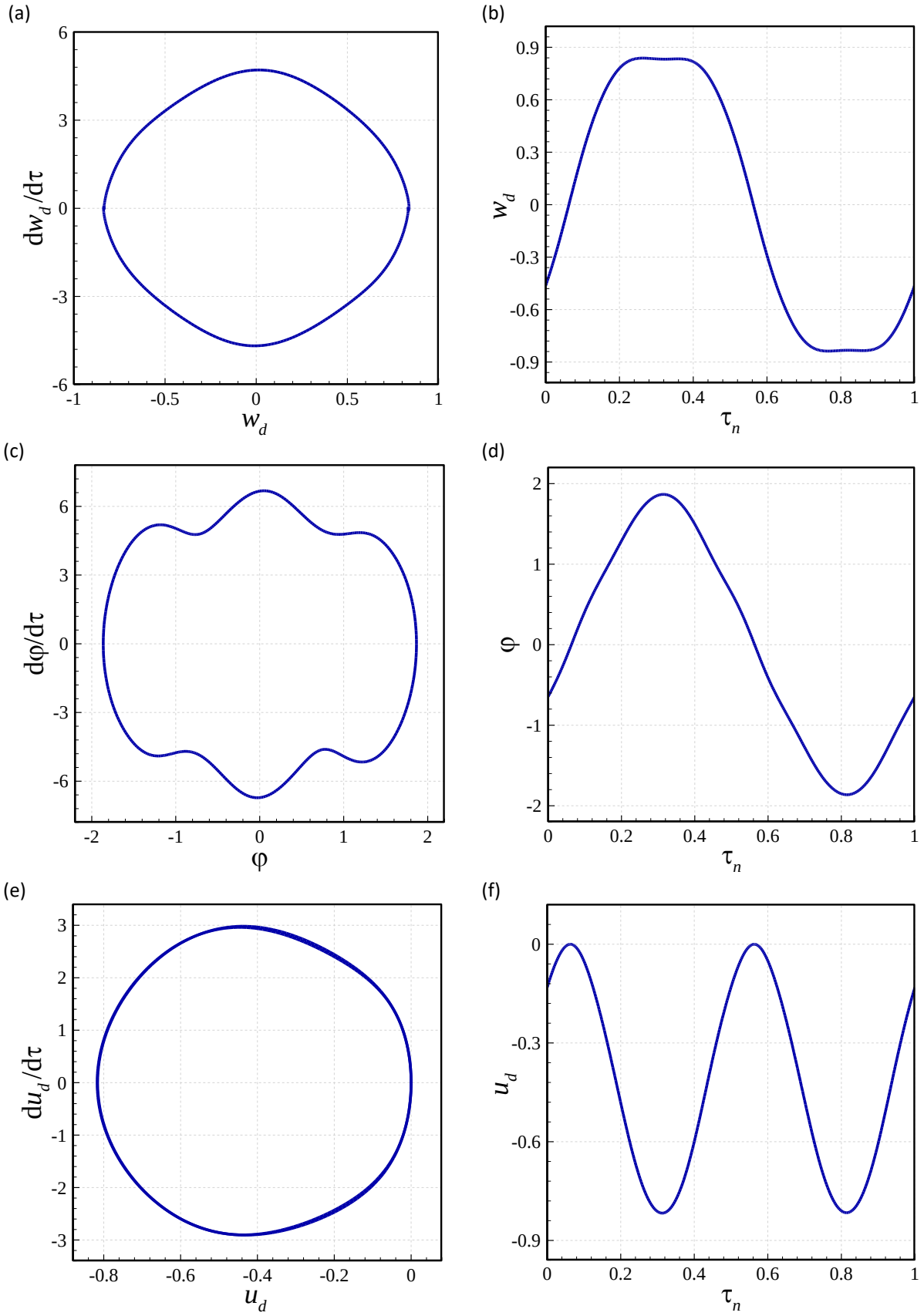

Fig.6. Dynamics of the cantilever of Fig. 4 in primary resonance when Ω_0/ω_1=1.0256; (a, b) phase-plane and time trace of w at tip, respectively; (c, d) those of φ at tip, respectively; (e, f) those of u at tip, respectively. τ_n : normalised time relative to the oscillation period.

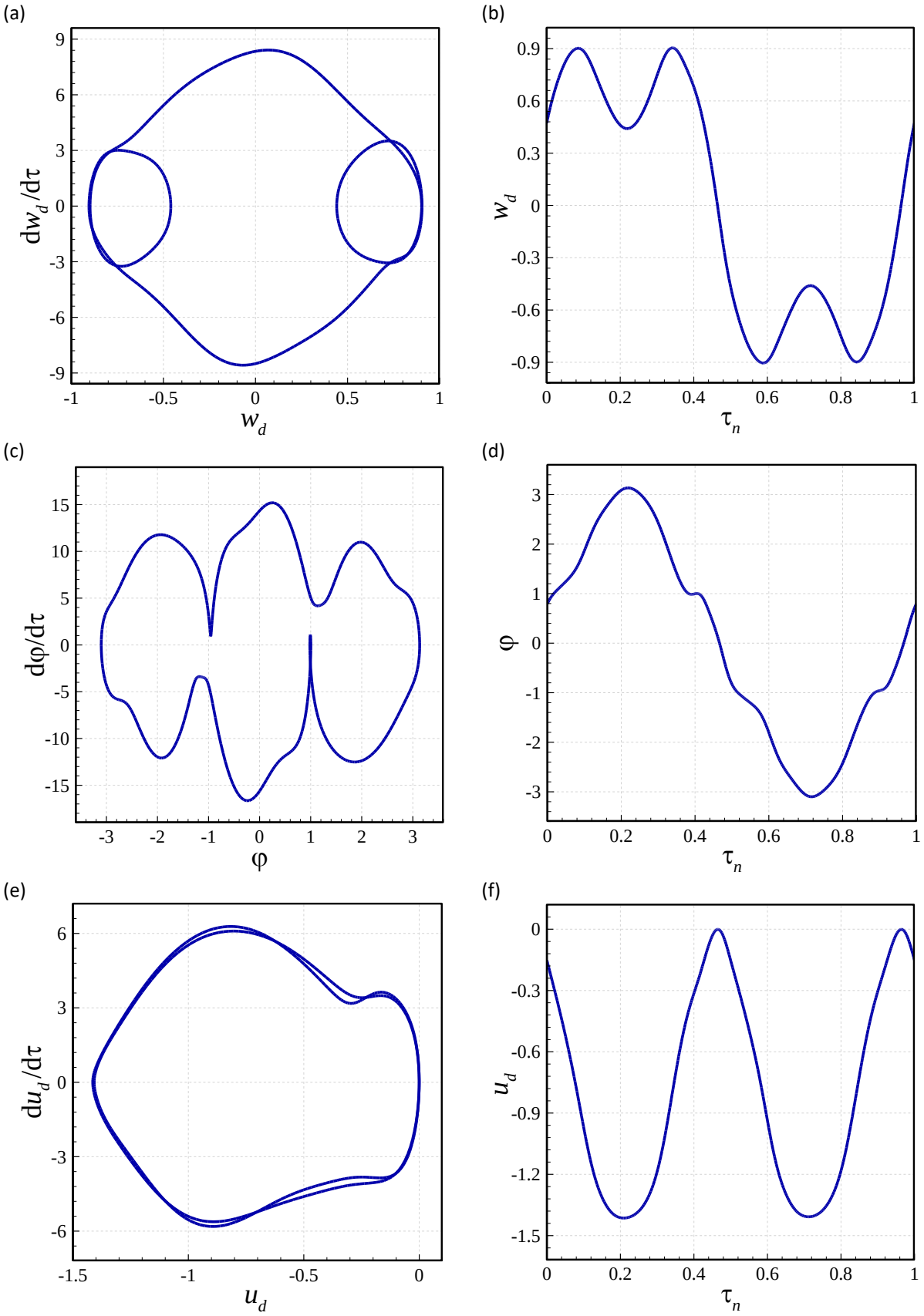

Fig.7. Dynamics of the cantilever of Fig. 4 in parametric resonance when Ω_0/ω_1=2.0779; (a, b) phase-plane and time trace of w at tip, respectively; (c, d) those of φ at tip, respectively; (e, f) those of u at tip, respectively. τ_n : normalised time relative to the oscillation period.

(a)

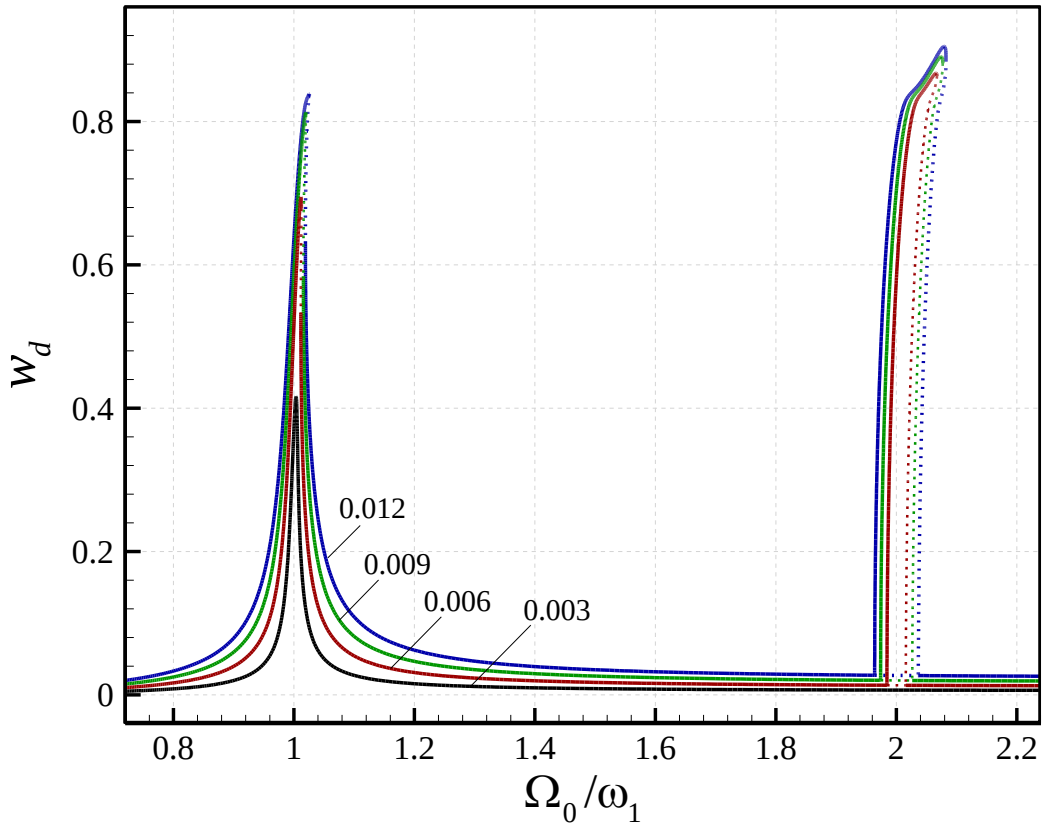
0.8
0.6
0.4
0.2
0
w_d
0.012
0.009
0.006
0.003
0.8
1
1.2
1.4
1.6
1.8
2
2.2
Ω_0/ω_1

(b)

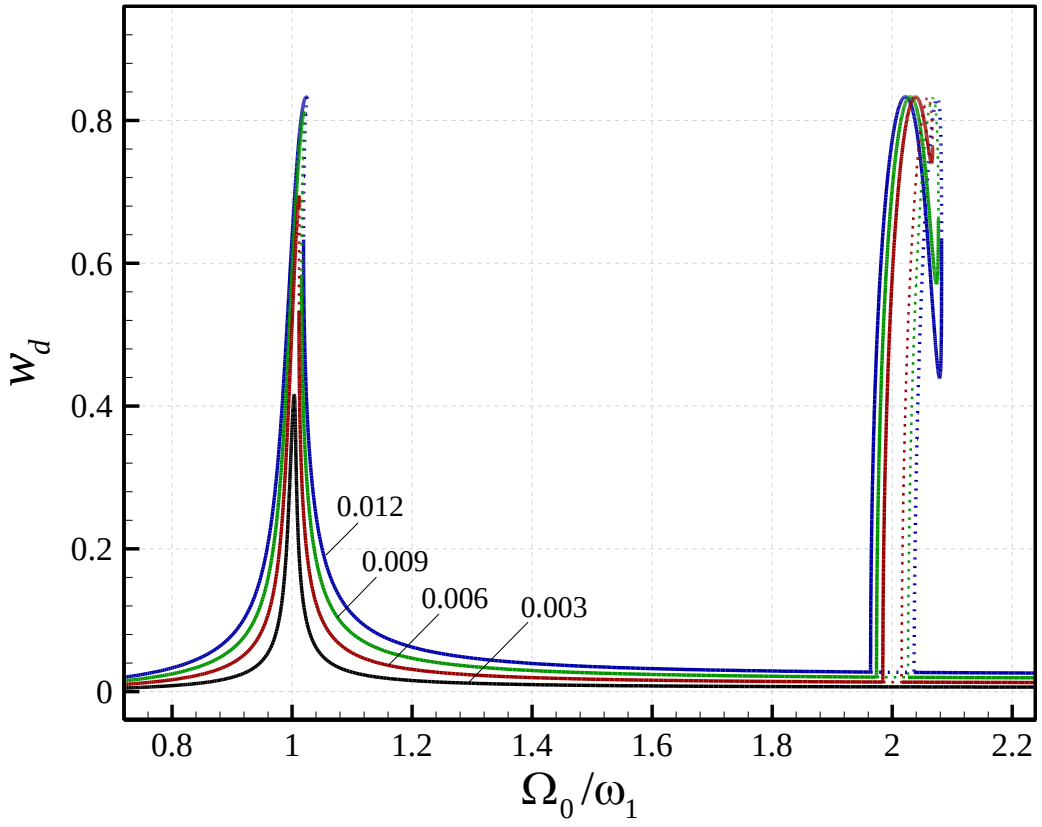
0.8
0.6
0.4
0.2
0
w_d
0.012
0.009
0.006
0.003
0.8
1
1.2
1.4
1.6
1.8
2
2.2
Ω_0/ω_1

(c)

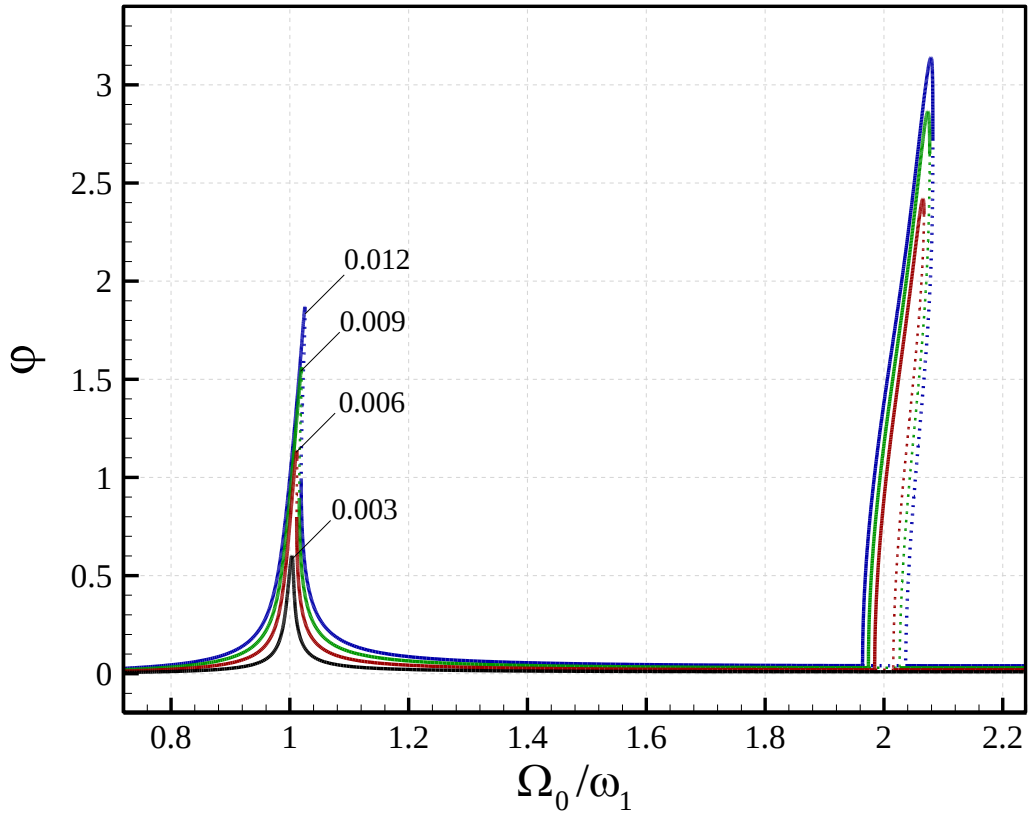

(d)

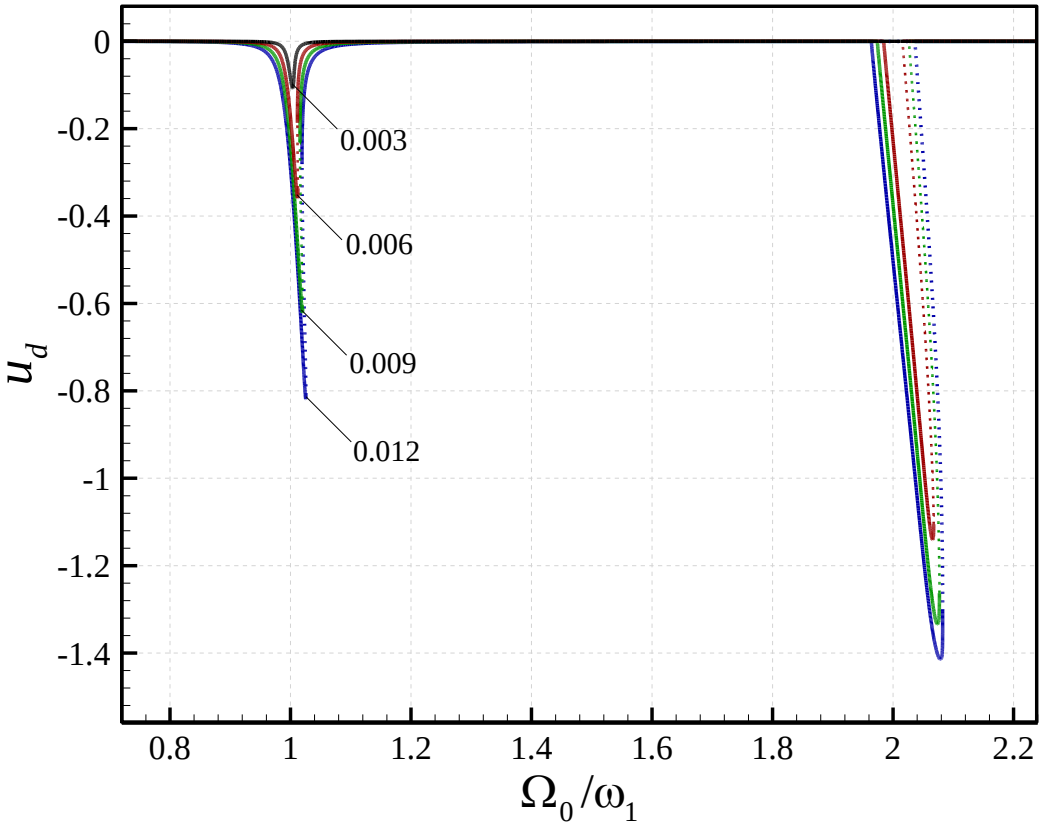

Fig.8. Large-amplitude oscillations of the cantilever under various coupled base motion amplitudes in primary and parametric resonance regions; (a) maximum transverse displacement at tip; (b) tip transverse displacement at the time of maximum tip rotation; (c) maximum rotation at tip; (d) maximum axial displacement at tip. The base motion amplitude is denoted on the curves noting that W_0=U_0 for all cases.

(a)

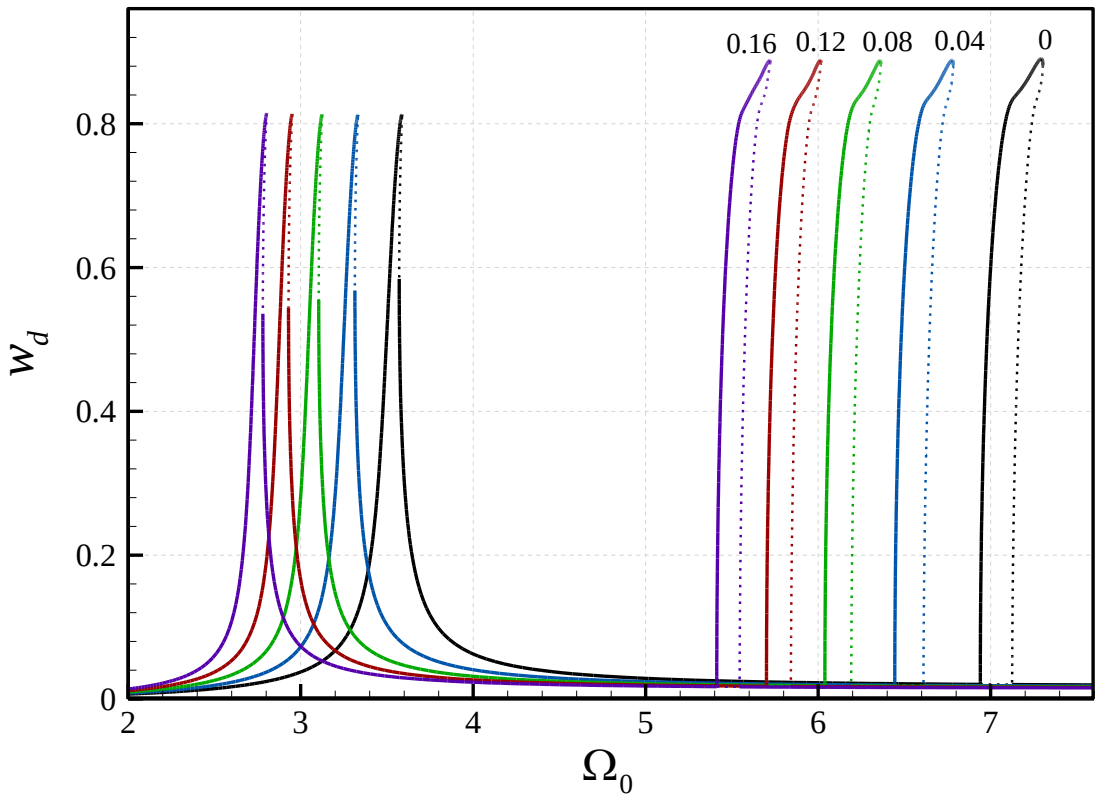
0.16
0.12
0.08
0.04
0
0.8
0.6
0.4
0.2
0
w_d
2
3
4
5
6
7
Ω_0

(b)

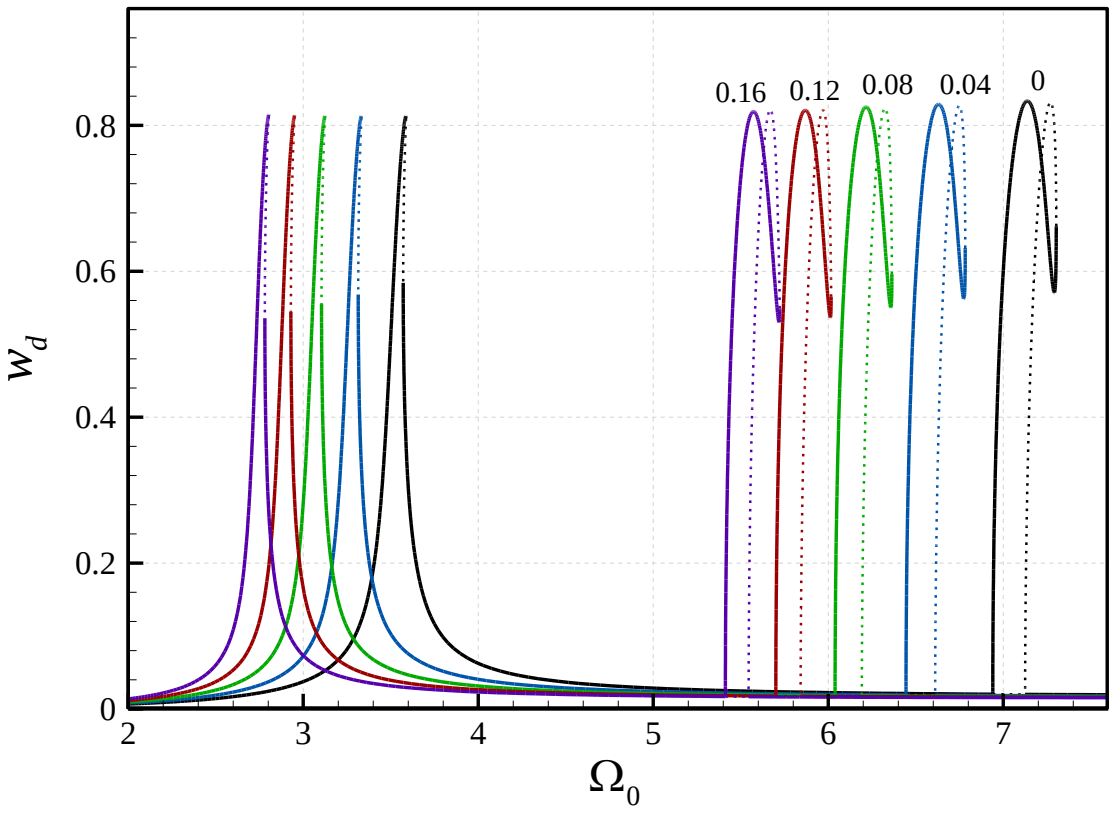
0.16
0.12
0.08
0.04
0
0.8
0.6
0.4
0.2
0
w_d
2
3
4
5
6
7
Ω_0

(c)

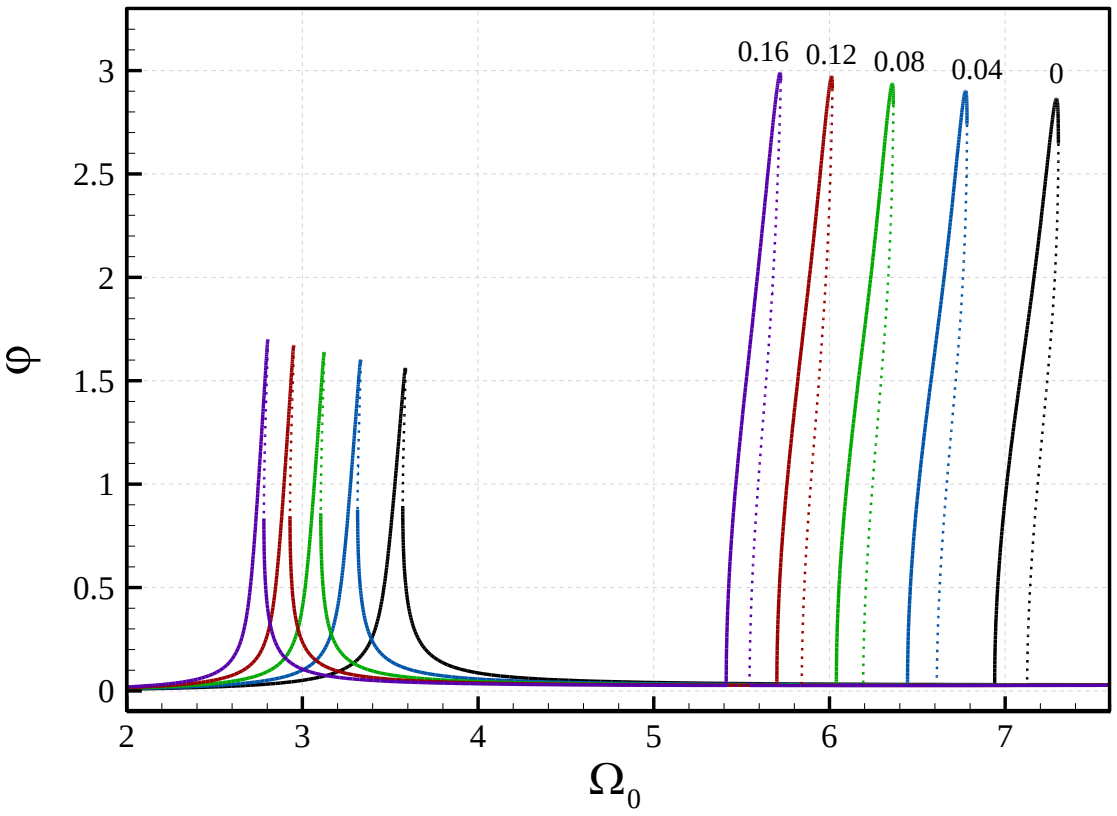

(d)

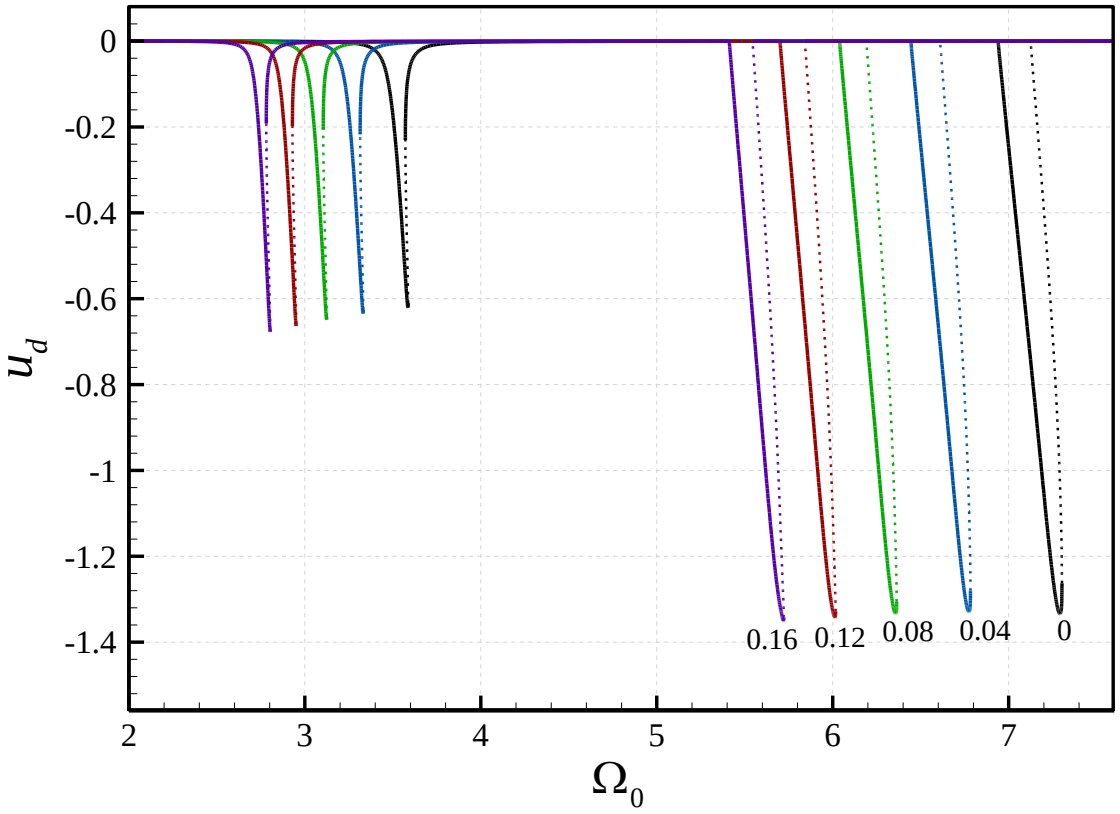

Fig.9. Tip mass ratio (χ) effect on oscillations of the cantilever under coupled base motions in primary and parametric resonance regions; (a) maximum transverse displacement at tip; (b) tip transverse displacement at the time of maximum tip rotation; (c) maximum rotation at tip; (d) maximum axial displacement at tip. W_0=U_0=0.009 for all cases.

(a)

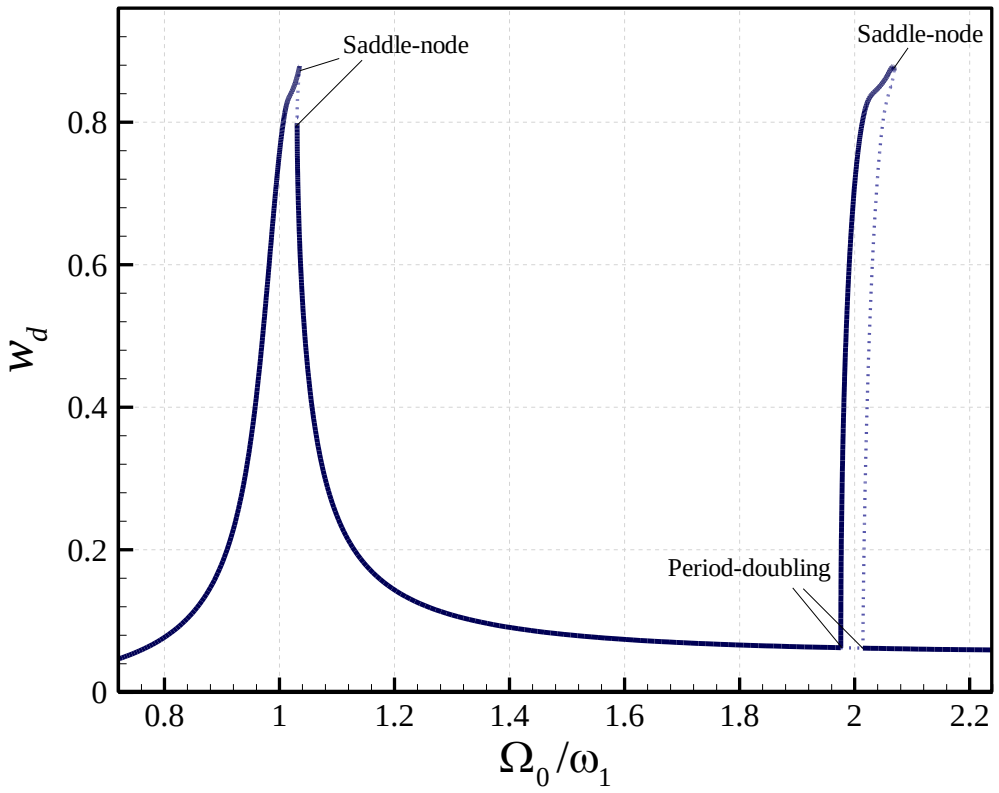
Saddle-node
Saddle-node
Period-doubling
0.8
0.6
0.4
0.2
0
w_d
0.8
1
1.2
1.4
1.6
1.8
2
2.2
Ω_0/ω_1

(b)

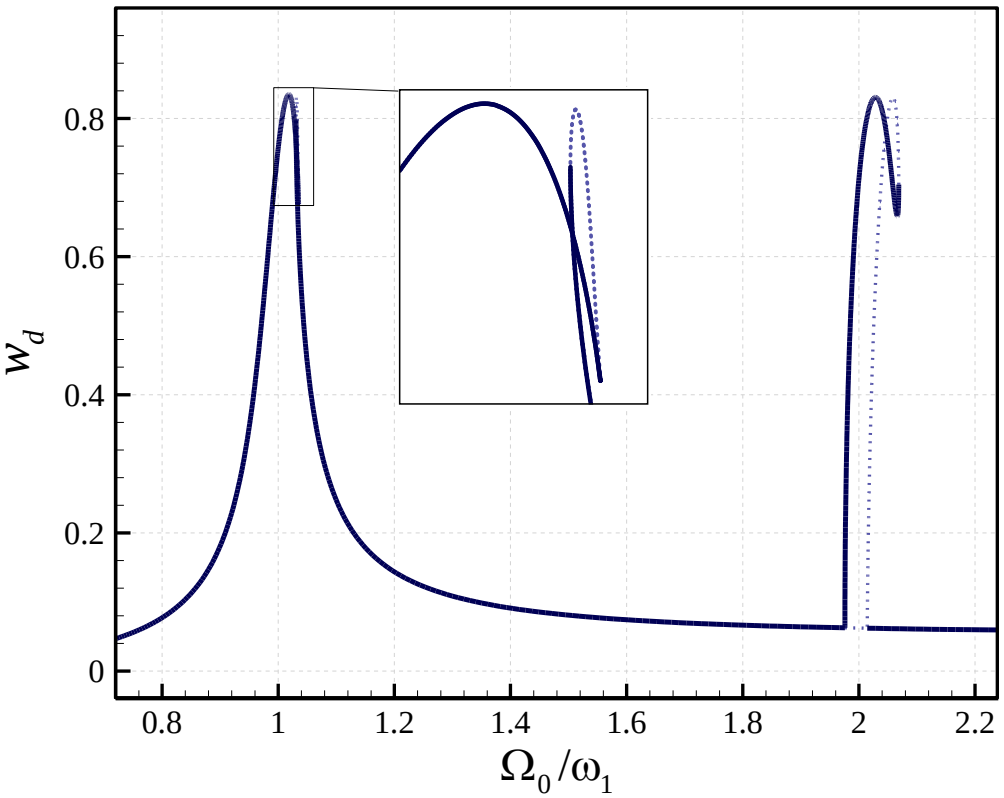
0.8
0.6
0.4
0.2
0
w_d
0.8
1
1.2
1.4
1.6
1.8
2
2.2
Ω_0/ω_1

(c)

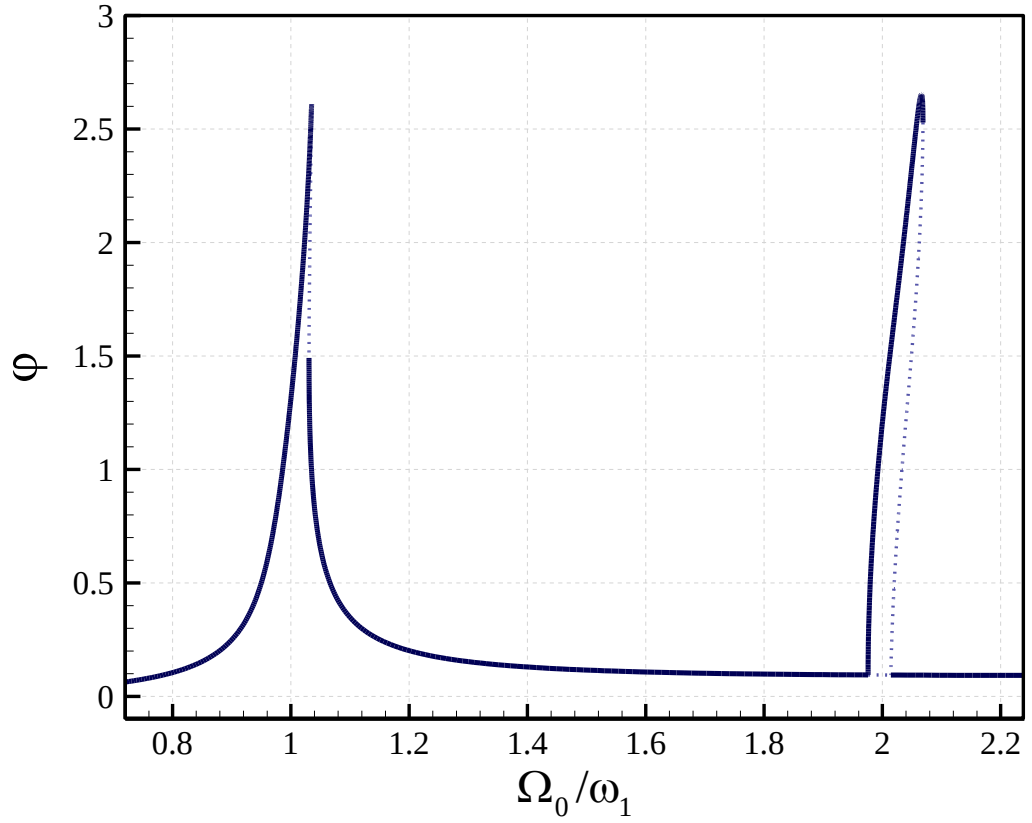

(d)

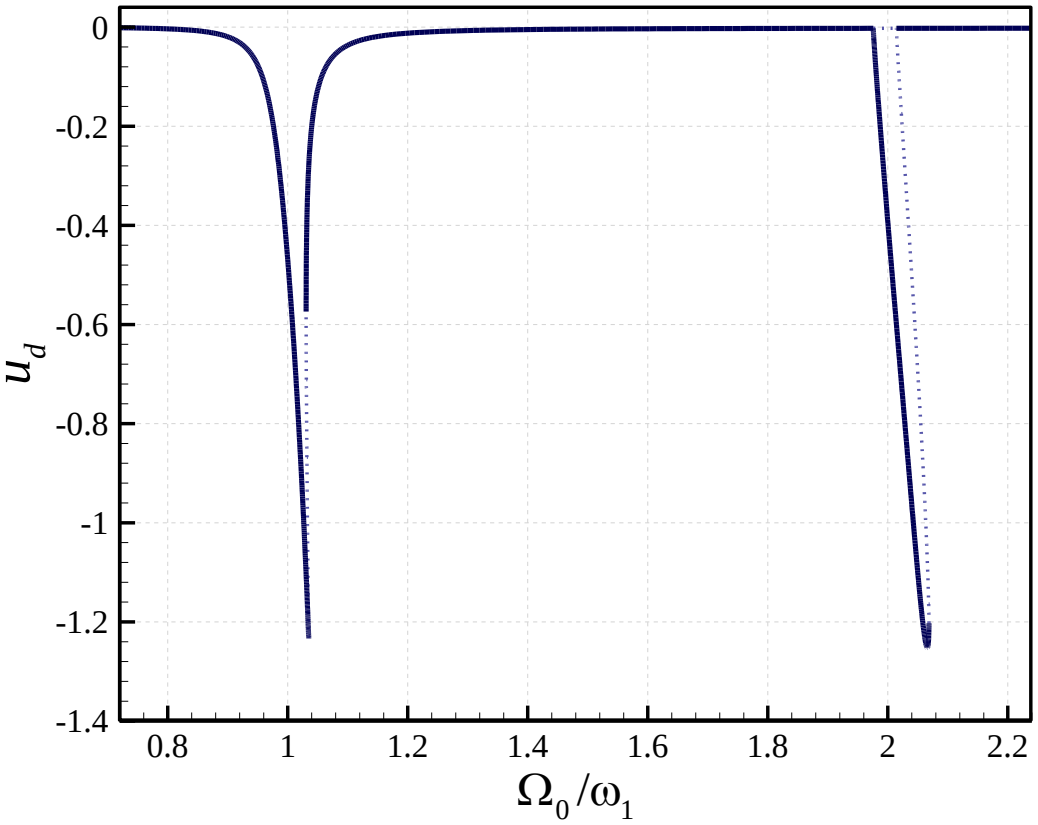

Fig.10. Large-amplitude oscillations of the cantilever under coupled base motions in primary and parametric resonance regions; (a) maximum transverse displacement at tip; (b) tip transverse displacement at the time of maximum tip rotation; (c) maximum rotation at tip; (d) maximum axial displacement at tip. W_0=0.028 and U_0=0.007.

(a) (b)

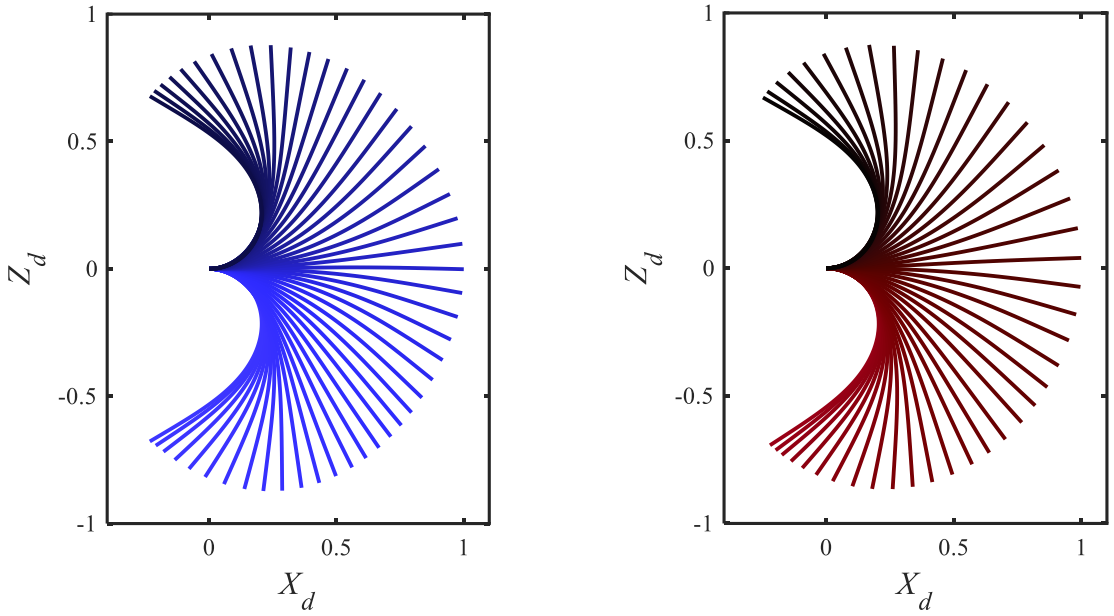

Fig.11. Oscillations of the cantilever of Fig. 10; (a) primary resonance response at Ω_0/ω_1=1.0351 and (b) parametric resonance response at Ω_0/ω_1=2.0667.

(a)

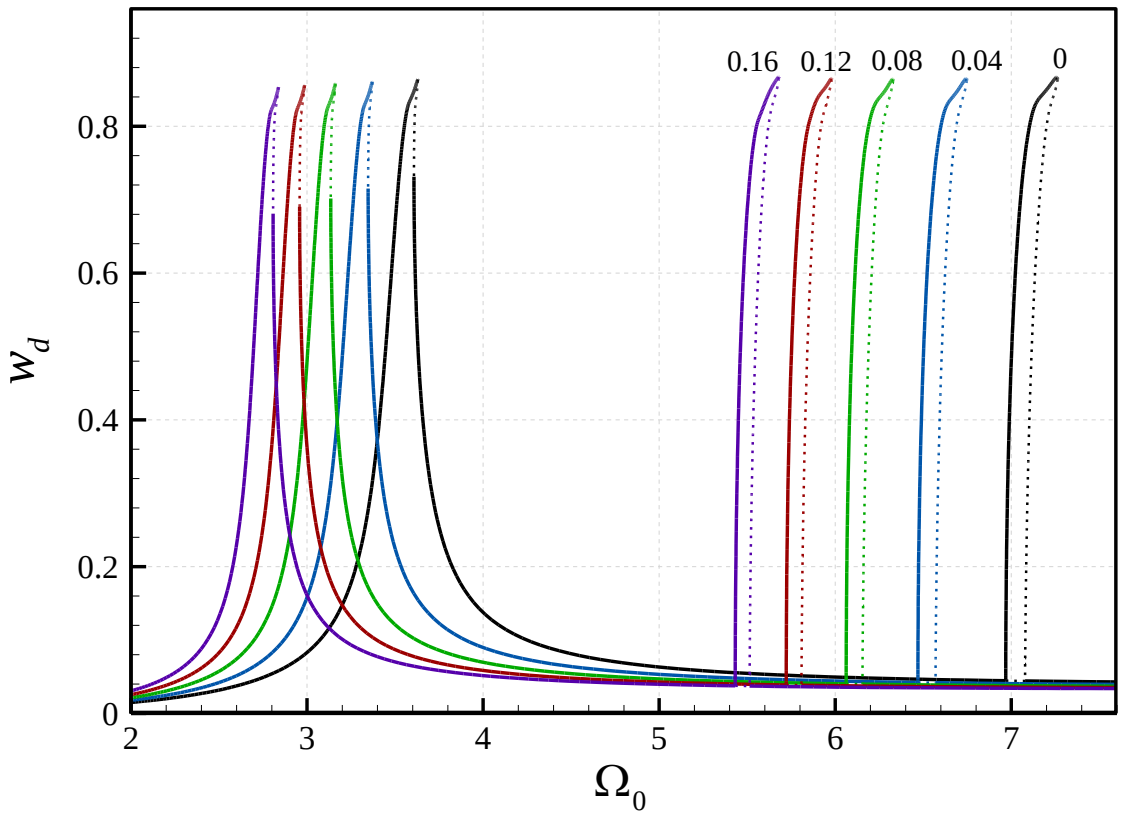
0.16
0.12
0.08
0.04
0
0.8
0.6
0.4
0.2
0
2
3
4
5
6
7
w_d
Ω_0

(b)

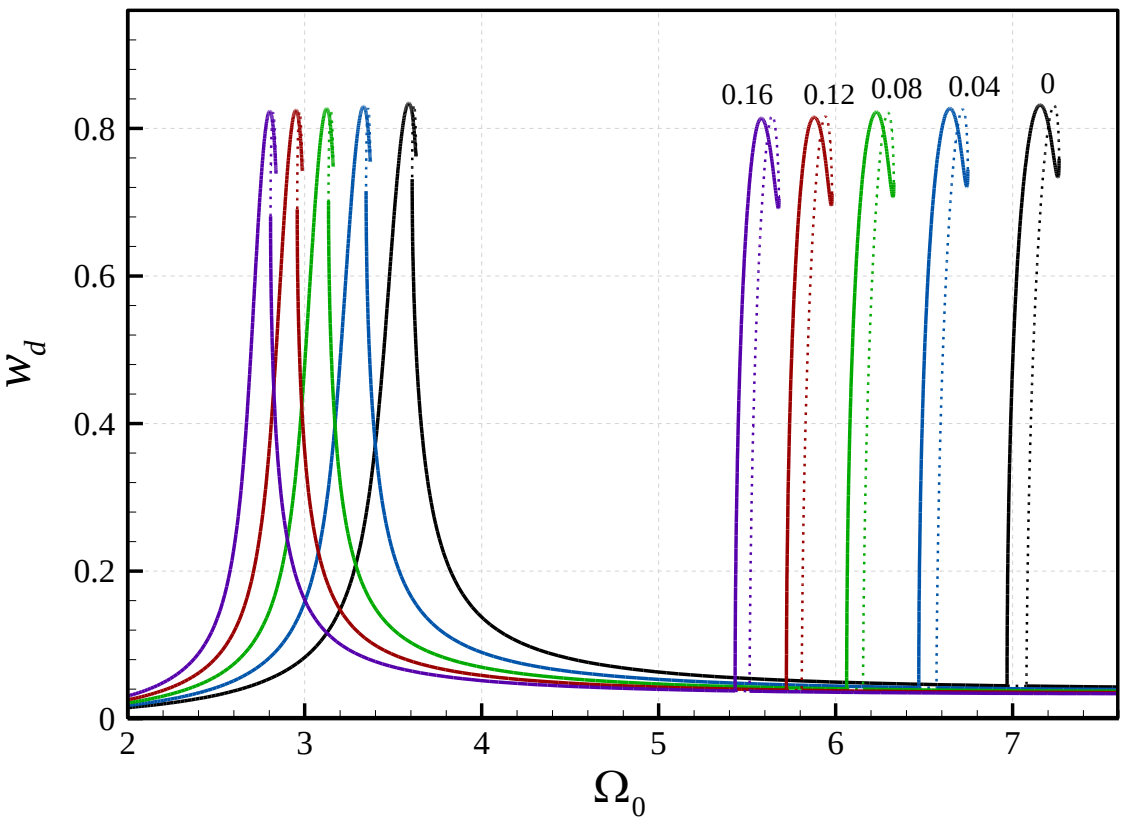
0.16
0.12
0.08
0.04
0
0.8
0.6
0.4
0.2
0
2
3
4
5
6
7
w_d
Ω_0

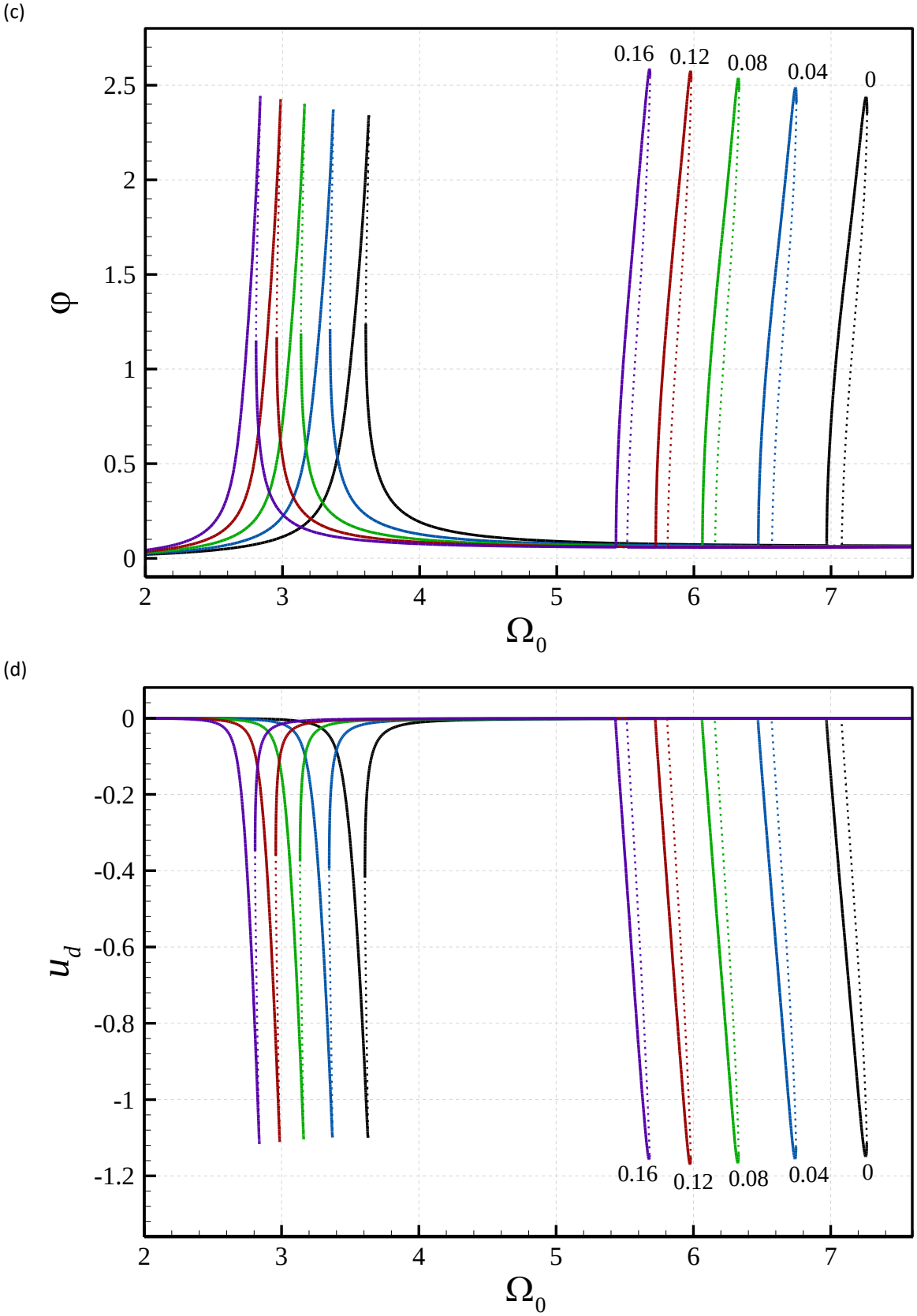

Fig.12. Tip mass ratio (χ) effect on oscillations of the cantilever under coupled base motions in primary and parametric resonance regions; (a) maximum transverse displacement at tip; (b) tip transverse displacement at the time of maximum tip rotation; (c) maximum rotation at tip; (d) maximum axial displacement at tip. W_0=0.020 and U_0=0.006 for all cases.